Continuous monitoring of basil (Ocimum basilicum L.) topology based on partial 4D point clouds

Auteur : Bouvry, Arnaud
Promoteur(s) : Lebeau, Frédéric; De Cock, Nicolas
Faculté : Gembloux Agro-Bio Tech (GxABT)
Diplôme : Master en bioingénieur : sciences et technologies de l'environnement, à finalité spécialisée
Année académique : 2016-2017
URI/URL : http://hdl.handle.net/2268.2/3010

Continuous monitoring of basil (*Ocimum basilicum L.*) topology based on partial 4D point clouds

Arnaud BOUVRY

Continuous monitoring of basil (*Ocimum basilicum L.*) topology based on partial 4D point clouds

Arnaud BOUVRY

Remerciements

Je voudrais remercier toutes les personnes qui m'ont amené où je suis aujourd'hui, qui m'ont soutenu et qui me sont venues en aide au cours de ce travail de fin d'études.

Merci à mes parents, sans qui je n'aurais pas eu la chance de vivre l'aventure de l'université et qui m'ont supporté à travers les différentes épreuves que j'ai pu y rencontrer.

Merci à Laura, pour son soutien indéfectible au cours de ces six années.

Merci à Benoît, pour toutes les années passées ensemble à Gembloux, les sessions, les guindailles. Ta détermination a été un exemple pour moi.

Merci à tous les cokotteurs, les amis, les semaines au ski, l'aventure "Peyresq", sans lesquels Gembloux n'aurait pas été pareil.

Merci à M. Lebeau, Nicolas et Mathieu qui m'ont suivi dans le travail quotidien lié à ce travail de fin d'études.

Un merci tout particulier à Jean-François, qui a su m'apprendre tant de choses sur moi-même, mais aussi sur les autres, ainsi que pour son sens pratique qui m'a beaucoup aidé.

Merci à Rudy pour avoir réponse à toutes les questions qu'un étudiant en TFE au GR peut être amené à se poser, et à Olivier pour son aide ô combien précieuse dans la rédaction en LaTeX.

Merci à mes professeurs, qui ont su m'inculquer le savoir et les compétences qui m'ont permis d'effectuer ce travail.

Finalement, je remercie les membres du jury pour avoir accepté de m'évaluer dans le cadre de ce travail.

Abstract

Since phenomics constitutes a bottleneck in yield improvements, there is a growing need to develop new, automated phenotyping tools. To study plant topological phenotype, the focus was set on three dimensional measurements with the help of a low cost laser range sensor : the Intel RealSense SR300. The use of functional-structural plant modeling was introduced and used to represent plant architecture in a graphical way. The experiment was conducted on basil in a hydroponic system with controlled environment, with the design of a high-throughput phenotyping platform in mind. Such systems are often automated and deliver large quantities of data and results, thus highlighting key-elements of plant physiology easier than ever before. The performance of the phenotyping platform was deemed encouraging. The automated use of the SR300 was explored and opens the way to better performing phenotyping experiments. A calibration method was proposed and measurement quality was not perfect but shows promise, given a few refinements. A plant modeling tool with graphical representation capabilities is introduced, with long-term possibilities for model implementation. This study opens many perspectives in terms of phenotyping applications with the validation of a low-cost 3D sensor and the proposal of a functional structural modeling tool.

Résumé

A cause du goulot d'étranglement que constitue la phénomique dans la recherche en amélioration végétale, le besoin se fait sentir de développer de nouveaux outils automatisés de phénotypage. Dans le but d'étudier le phénotype topologique de plantes, l'accent a été mis sur des mesures en trois dimensions à l'aide du capteur low-cost Intel RealSense SR300. L'utilisation de la modélisation végétale fonctionelle-structurelle est introduite et utilisée pour représenter graphiquement une architecture végétale. L'expérimentation a pour objet du basilic en culture hydroponique avec environnement contrôlé, avec à l'esprit la conception d'une plate-forme de phénotypage à haut débit. De tels systèmes sont souvent automatisés et permettent de récolter de grandes quantités de données et de résultats, mettant ainsi en évidence des éléments clés de la physiologie végétale plus facilement que jamais auparavant. La performance de la plate-forme de phénotypage est jugée encourageante. L'utilisation automatisée de la SR300 a été explorée et ouvre la voie à des expériences de phénotypage plus performantes. Une méthode d'étalonnage a été proposée et la qualité de mesure, bien qu'imparfaite, est prometteuse moyennant quelques améliorations techniques. Un outil de modélisation avec des possibilités de représentation graphique est proposé, avec la possibilité à long terme d'y intégrer de nouveaux modèles. Cette étude ouvre de nombreuses perspectives en termes d'applications de phénotypage, avec la validation d'un capteur 3D au prix abordable et la proposition d'un outil de modélisation performant.

Contents

List of Figures

List of Tables

Acronyms

ASIC   Application Specific Integrated Circuit
CCD   Charge Coupled Device
CEA   Controlled Environment Agriculture
CMOS   Complementary Metal Oxide Semiconductor
DAS   Days After Sowing
DPI   Dots Per Inch
EC   Electrical Conductivity
FOV   Field Of View
HSV   Hue Saturation Value
HVAC   Heat, ventilation and air-conditioning
IR   Infra Red
LED   Light-emitting Diode Detection And Ranging
LIDAR   Light Detection And Ranging
MTG   Multiscale Tree Graph
PA   Precision Agriculture
PCB   Printed Circuit Board
PNG   Portable Network Graphics
PPM   Parts Per Million
RGB   Red Green Blue
RGB-D   Red Green Blue-Depth
ROI   Region Of Interest
SDK   Software Development Kit
TOF   Time Of Flight
UV   Ultraviolet
XPS   Extruded Polystyrene foam

Chapter 1

Introduction

Whether to face the challenges of feeding the ever growing world population (Godfray et al., 2012) — with an estimation close to 10 billion individuals in 2050 (United Nations, 2017), to increase benefits or to create new agricultural systems, research in plant physiology is essential to understand the interactions between plants genome, phenome and environment. To do so, the scientific community has had many tools at its disposal, with recent dramatic advances in genomics through DNA sequencing. Now, phenomics is constituting a bottleneck to advances in yield improvements (Fahlgren, Gehan, & Baxter, 2015; Fiorani & Schurr, 2013).

To conduct efficient phenotyping experiments and platform design, it is essential to correctly identify relevant parameters to be measured, design automated cultivation systems, monitor environmental variables and gather data efficiently (Fiorani & Schurr, 2013). It is with those aims that high-throughput phenotyping platforms are designed.

This work falls in the scope of plant topological traits monitoring through image-based processes. Image-based phenotyping is a wide terminology that actually encompasses several techniques, based on the behavior of plant material in different growth and illumination conditions, with various scopes and purposes. These different techniques are summarized in the review of L. Li, Zhang, and Huang (2014) and rely on visible light, fluorescence, thermal, near infrared, hyperspectral, 3D, or laser imaging. Some authors even explore the use of medical imaging techniques such as magnetic resonance imaging (MRI), positron emission tomography (PET) or computed tomography (CT).

The future is bright for this field of study as recent years have seen advances in hardware and software performance and availability. Indeed, sensors are becoming more affordable with several papers exploring the use of cheap, consumer-grade red-green-blue (RGB) cameras, 3D scanners or depth cameras to study plant architecture (Azzari, Goulden, & Rusu, 2013; Chéné et al., 2012; Paulus, Behmann, Mahlein, Plümer, & Kuhlmann, 2014). On the other hand, many commercial and open-source phenotyping tools exist. The Plant Image Analysis database (Lobet, Draye, & Périlleux, 2013) is a repository of such image analysis tools designed specifically for plant phenotyping.

Much like phenotyping techniques are varied, so are their scopes. While some are limited to the individual plant, others take phenotyping to the field (Dong, Burnham, Boots, Rains, & Dellaert, 2016).

In the present case, a hydroponic cultivation system was designed in a controlled environment, together with an automated acquisition system. The experiment was conducted in a controlled environment on a dozen of basil plants. The purpose was to explore the possibility to study plant topology with the help of the Intel RealSense SR300 depth camera and to determine what methodology or software could be used to make the best use of the measured parameters.

Chapter 2

Bibliographic Review

2.1 Plant phenotyping

L. Li et al. (2014) define plant phenotyping as "*the comprehensive assessment of complex plant traits such as growth, development, tolerance, resistance, architecture, physiology, ecology, yield, and the basic measurement of individual quantitative parameters that form the basis for more complex traits*". Characterization of said processes relies on the precise measurement of several parameters in specific environmental conditions.

As the scope of this work focuses on image-based phenotyping, a short review of existing techniques will be realized. The purpose of image-based phenotyping is to take measurements in a non-destructive manner, based on the behavior of photons in relation with plant material : photon reflection, absorption or transmission, in different illumination conditions (Figure 2.1). An automation component is also present in image acquisition and treatment, as computer vision allows development of algorithms to automatically operate equipment and extract results from data.
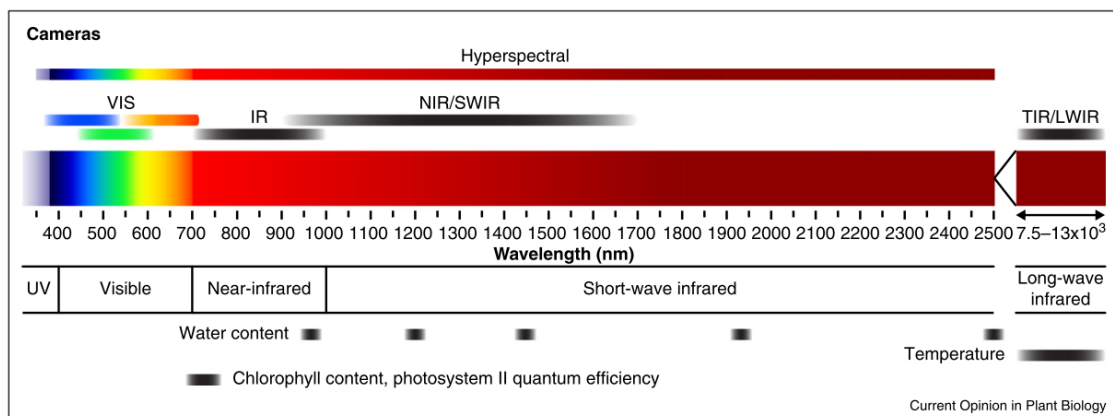
Figure 2.1 – *Ranges of cameras and sensors used in plant phenotyping (Fahlgren et al., 2015).*

Visible light Born of the simplest imaging technique used for plant phenotyping, visible-light images are intended to mimic human perception. Sensors used in this scope are most commonly silicon complementary metal oxide semiconductor (CMOS) or charge coupled device (CCD) arrays, sensitive in the visible range of the light spectrum (400 to 700 nm).

Images are acquired in top-view for plants presenting a rosette architecture (*Arabidopsis*), and sometimes complementary side-views in the case of more complex architecture. Raw data is usually presented in the form of matrices with 3 channels : red, green and blue. Each channel holds the intensity of light in the corresponding wave band.

A few examples of current applications are biomass estimations (Arvidsson, Pérez-Rodríguez, & Mueller-Roeber, 2011; Golzarian et al., 2011), yield traits, plant organs morphology, root architecture, projected leaf area (L. Li et al., 2014). Simple parameters estimations display a high coefficient of determination with respect to reference measurements. The advantage of such an approach is that data can be easily acquired in large scale experiments, sometimes in a fully automated manner. This gain in time and resources management enables the use of large populations and a genetic approach to plant phenotyping, as Chen et al. (2014) did in an experiment where 312 plants were monitored over the course of seven weeks using an automated conveyor belts system.

Visible light imaging is compatible with both controlled environment and field agriculture. However, the technique faces some limitations, especially in the field, where illumination conditions are dependent on time of the day, season and cloud coverage. Background elimination can be achieved with the help of image transformations (Woebbecke, Meyer, Von Bargen, & Mortensen, 1995). In the field, visible imaging is used to quantify canopy color and coverage (L. Li et al., 2014).

Fluorescence imaging   Fluorescence imaging is oriented towards the observation of metabolic status of plant, especially photosynthesis related processes as the typical fluorescing part of plant material is the chlorophyll complex (L. Li et al., 2014). It originated from the findings of Kautsky and Hirsch (1931) on the difference in fluorescence in dark-adapted leaves, highlighting the correlation between fluorescence rate and carbon dioxide assimilation. In fluorescence imaging, surfaces are irradiated with context-specific light and measurements aim at the capture of re-emitted light fractions which depend on the status of the plant (Baker, 2008). Multicolor fluorescence imaging uses ultraviolet (UV) irradiation and allows the recording of plant material response in four spectral bands, namely blue (440 nm), green (520 nm), red (690 nm) and far-red (740 nm). These responses inform on various plant components and associated processes, and their simultaneous analysis can provide thorough indicators of stress or even chloroplast content (L. Li et al., 2014).

This technique is obviously of primary interest in disease detection, and in both biotic and abiotic stress response measurement. To sum up, it is a widespread tool to assess plant metabolic performance, submitted to various stress and other particular conditions. Power requirements and specific irradiation conditions make it a suitable tool for controlled environment experiments, but field applications are not yet suited for large-scale experiments (L. Li et al., 2014).

Thermal imaging   Thermal imaging is used to visualize thermal radiations at the surface of framed objects, i.e. leaf surface and canopy. Common operating wavelengths for thermal imaging are 3 to 5 µm and 7 to 14 µm. Recent developments in thermal imaging

sensors have brought a generation of cameras with thermal sensitivity the order of the millikelvin.

Because of the close relationship between leaf temperature and evapotranspiration, it is used to study plant-water relations. A direct application of such measurement lies in drought-resistant genotypes breeding programs (Jones et al., 2009). It is adapted to both field and controlled environment use but requires heavy procedures of calibration, and the geometry of analyzed plants must be taken into account in the interpretation of measurements (L. Li et al., 2014).

Hyperspectral imaging   With cameras able to discern hundreds of spectral bands ranging from 350 to 2500 nm, with a resolution of the order of the nanometer, hyperspectral imaging enables the extraction of information otherwise lost in the process of broader band images acquisition (Fahlgren et al., 2015). It relies on interaction of solar radiation with plant canopy. In the visible spectrum, surface reflectance is especially low due to the absorption of light by leaf pigments and presents a peak of reflectance in the green region of the visible spectrum (L. Li et al., 2014). The abundance of wavelengths allows the computation of various vegetation indices (ratio of one on the other, difference between two spectral bands) which, with proper calibration, can predict phenotypic characteristics such as yield (Marti, Bort, Slafer, & Araus, 2007), crop response to stresses and leaf nitrogen content (Leemans, Marlier, Destain, Dumont, & Mercatoris, 2017).

The downside of hyperspectral imaging lies in the slowness of image acquisition, and the interpretation of data poses supplementary challenges to researchers as the volume of data grows with each extra band.

3D imaging   3D plant phenotyping is the particular category in which the present work falls. Sensors capturing 3D data are laser scanners (or structured light depth cameras), stereo vision cameras and time of flight (TOF) cameras.

Laser scanners rely on active triangulation. A pattern is projected onto the scene, and signal processing provides a depth map of the framed area. Section 2.4 gives more detail about this technology since it is the category that the sensor of interest of this study falls into.

Stereo cameras generally have two sensors mounted close to each other and partially framing the same scene. However, they sometimes are made of 3 cameras, or only one for "*Structure From Motion*" stereo cameras where a static scene is captured by a number n of successive frames from different positions (Zanuttigh et al., 2016).

As for TOF cameras, their applications in plant phenotyping remain limited because of comparatively low resolution and sensitivity to outdoor illumination (L. Li et al., 2014).

The purpose of 3D imaging is mainly to study plant architecture. Measurements range from topographic maps to height or volume measurements, enabling the estimation of biomass production or canopy cover. Point cloud analysis can provide rich informations on plant growth (Paulus, Schumann, Kuhlmann, & Léon, 2014) and surface features based algorithms allow the segmentation of plant organs (Paulus, Dupuis, Mahlein, & Kuhlmann, 2013). Various scales have been explored, from the 3D mapping of single, small plants to

the use of aerial mounted stereo cameras for growth estimations by Rovira-Más, Zhang, and Reid (2005) or aerial use of light detection and ranging (LIDAR) to characterize forest coverage.

Y. Li et al. (2013) and Paproki, Sirault, Berry, Furbank, and Fripp (2012) even go further by bringing phenotyping in the 4th dimension, by establishing techniques of continuous 3D monitoring, thus adding the time axis to spatial measurements.

Table 2.1 – *Comparison of image-based phenotyping techniques (L. Li et al., 2014).*

Imaging Techniques	Sensor	Resolution	Raw Data	Phenotype Parameters	Examples of Species	Imaging Environment
Visible light imaging	Cameras sensitive in the visible spectral range	whole organs or organ parts, time series	Gray or color value images (RGB channels)	Projected area, Growth dynamics, Shoot biomass, Yield traits, Panicle traits, Root architecture, Imbibition and germination rates, Early embryonic axis growth, Height, Size morphology, Flowering time	*Arabidopsis thaliana* [15,27,42,43]; Barley [13]; Rice [11,18,44,45]; Legume *Medicago truncatula* [46]; Maize [47,48]; Bean [49]	Controlled environment; field
Fluorescence imaging	Fluorescence cameras and setups	Whole shoot or leaf tissue, time series	Pixel-based map of emitted fluorescence in the red and far-red region	Photosynthetic status (variable fluorescence), quantum yield, non-photochemical quenching, leaf health status, shoot architecture	Wheat [50,51]; *Arabidopsis* [14,52–54]; Natural grassland, winter wheat, corn [55]; Barley[56,57]; Bean[58]; Sugar beet [59]; Tomato [60]; Chicory plant [61];	Controlled environment; Field
Thermal imaging	Near-infrared cameras,	Pixel-based map of Surface temperature in the infrared region	Whole shoot or leaf tissue, time series	Canopy or leaf temperature, insect infestation of grain	Barley [56]; Wheat [56,62]; Maize [63]; Grapevine [64]; Rice [64];	Controlled environment; Field
Near infrared imaging	Near-infrared cameras, multispectral line scanning cameras, active thermography	Continuous or discrete spectra for each pixel in the near-infrared region	Time series or single-time-point analyses of shoots and canopies, single-point assessment of seeds	water content composition parameters for seeds, leaf area index	Rice[65–67]; Soybean [68]; Maize [69,70]; Barley [71]; Wheat [56]	Controlled environment
Hyperspectral imaging	Near-infrared instruments, spectrometers ,hyper spectral cameras, thermal cameras	Crop vegetation cycles, indoor time series experiments	Continuous or discrete spectra	Leaf and canopy water status; Leaf and canopy health status; panicle health status; leaf growth; Coverage density	Rice [72–76]; Wheat [50]; *Arabidopsis* [77]; Triticale [78]	Field; Controlled environment
3D imaging	Stereo camera systems; time-of-flight cameras	Whole-shoot time series at various resolutions	Depth maps	Shoot structure; leaf angle distributions; canopy structure; root architecture; Height	Soybean [39]; Rosebush; Maize [79]; Triticale [78]; Pepper [80]	Field; Controlled environment
Laser imaging	Laser scanning instruments with widely different ranges	Whole-shoot time series at various resolutions	Depth maps, 3D point clouds	Shoot biomass and Structure; leaf angle distributions; canopy structure; Root architecture; Height; Stem	Maize [81]; Sugar beet and wheat ears [82]; Triticale [78]; Barley [83]; Soybean [84];	Field; Controlled environment
MRI	Magnetic resonance imagers	200–500 μm; 1–600 s	Water(^{1}H) mapping	Morphometric parameters in 3D; Water content	Sugar beet [85]; *Hordeum spontaneum* and *Beta vulgaris* [86]; Bean [87]	Controlled environment
PET	Positron emission detectors for short-lived isotopes (e.g., $^{11}CO_2$)	1–2 mm; 10 s–20 min	Radiotracer mapping and coregistration with positron emission signals	Transport partitioning, sectorality, flow velocity	*Hordeum spontaneum* and *Beta vulgaris* [86]	Controlled environment
CT	X-ray computed tomography and X-ray digital radiography	100 μm and lower; hours	Voxels and tissue slices	Tillers; Morphometric parameters in 3D; grain quality	Rice [88]; Wheat [10,89–91]	Controlled environment

2.2 Functional structural plant modeling

Functional structural plant modeling is an approach used to study plant architecture and physiological processes through computer simulations. It differs from the general trend of crop growth models, that are generally process-based, in that it is developed with a strong structural component in mind and the relationship existing between plant architecture and physiological processes (Henke, Kurth, & Buck-Sorlin, 2016).

The work of Godin and Caraglio (1998) proposes a multi-scale approach to functional structural plant modeling, allowing to approach a new plant species without *a priori* on it's size or architecture. The multiscale tree graph (MTG) is indeed a tool fit to any plant species with any desired refinement level, describing the structure of plants in sets of components and the way these components are connected to each other. Characterizing said topology in a precise manner allows the study of plant physiology and growth process by exacerbating phenotypic traits that are not straightforward or obvious (Godin & Caraglio, 1998). To do so, the multiscale tree graph approach is based on graph theory. A graph h is defined as a pair $h = (V, E)$ where V is a finite set of vertices and E a finite set of edges. In the MTG formalism, those vertices correspond to components (i.e. leaves, stems, petioles, internodes, etc.) and the edges to the connections between those components (Figure 2.2).

(a) *Schematic tree structure.*

(b) *Corresponding tree graph.*
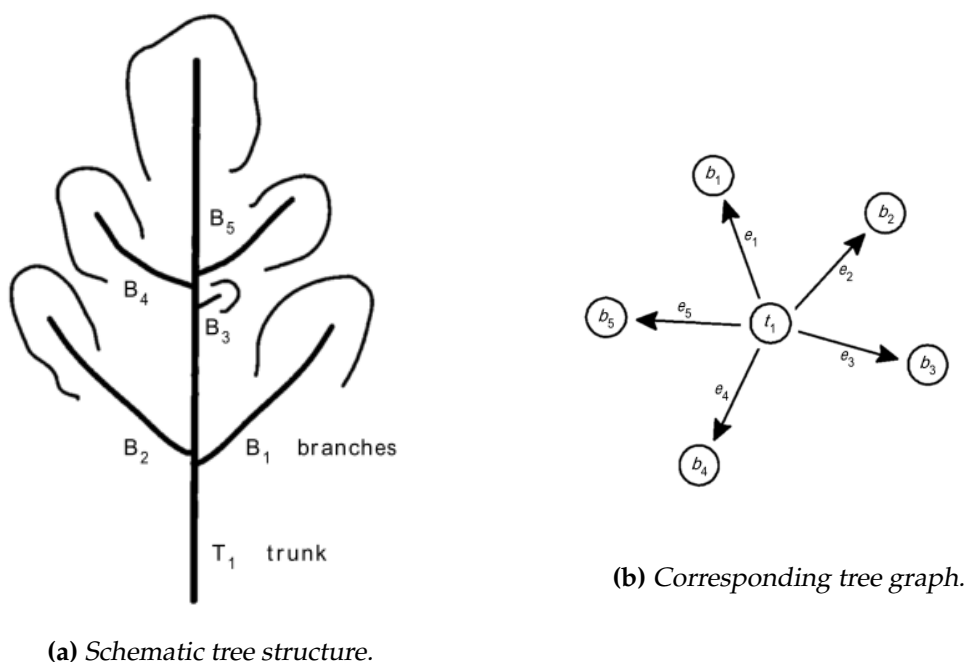
Figure 2.2 – *(a) Schematic structure of a tree and (b) the corresponding tree graph. The trunk is represented by the central vertex t_1 and the branches borne by the trunk are the linked vertices. The arrows in (b) are the edges of the graph (Godin & Caraglio, 1998).*

The identification and quantification of such topological traits constitutes a comprehensive and dynamic approach to plant form and development (Barthelemy & Caraglio, 2007). Numerous possible applications can be envisioned in botany and agronomy, regarding the development of plants based on endogenous processes and their response to external

variables (Barthelemy & Caraglio, 2007; Najla et al., 2009).

The outputs of such models are sets of morphological, topological parameters, represented in a graphical way as per example in the software AMAPstudio developed by Griffon and de Coligny (2014), providing computed representations consistent with field observations (Figure 2.3).

Figure 2.3 – *Example of simulated plant architecture within the AMAPstudio software (Griffon & de Coligny, 2014).*

2.3 Basics of imaging systems (Zanuttigh et al., 2016)

This section is a simplified overview of the basic principles on which imaging systems work and that are necessary for the proper understanding of the rest of this thesis. It is mostly based on the chapter "*Basics of Imaging Systems*" in Zanuttigh et al. (2016).

The pinhole camera model is the abstract simplification of the geometry of a camera (Figure 2.4). It defines a 3D *Camera Coordinates System* with axes x, y and z and the origin located at the pinhole, called the *center of projection*, on the face of the camera. Parallel to the face of the camera is the *sensor* (also called *film* or *image plane*). The *focal length* is the distance separating the pinhole from the sensor plane, and the *principal point* or *optical center* is the projection of the pinhole on the sensor, normal to the sensor plane.

The sensor is made of an array of photoelectric conversion units converting photons into electric signals, based on CCD or CMOS technology (Fraden, 2010). These electronic signals become values that are stored in an array and become pixel values in an image. From a mathematical perspective, the relationship between pixel coordinates on the sensor array $p = [u, v]^T$ and points coordinates in real-world coordinates $P = [x, y, z]^T$ comes from triangle similarity (Equation 2.1, Figure 2.5).

(b) *Focal length*

(c) *Principal point*
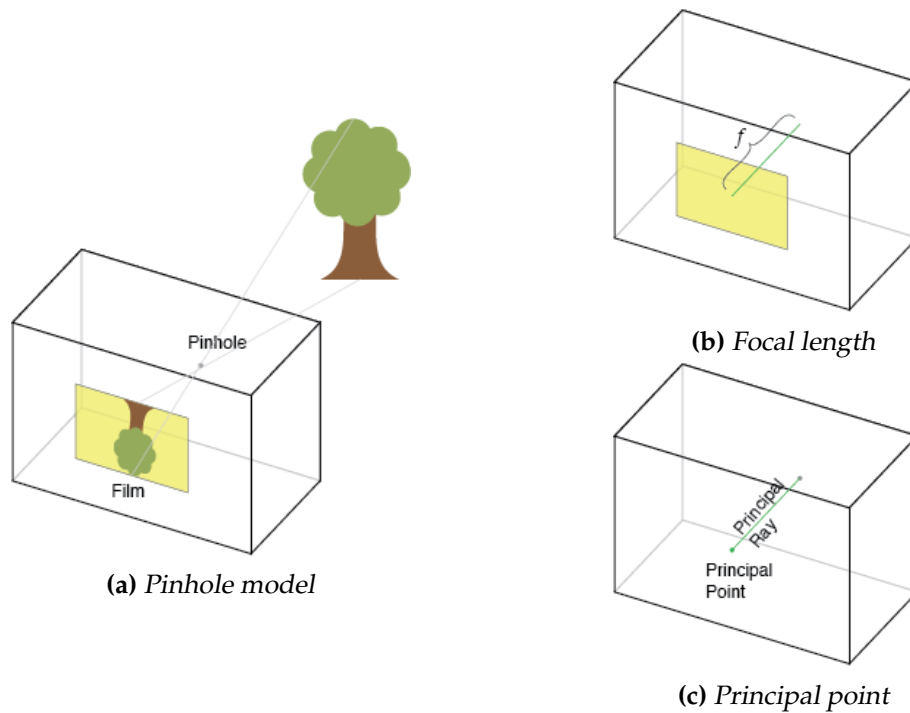
(a) *Pinhole model*

Figure 2.4 – *Simple representation of the pin-hole model and it's main components, the focal length (a) and the principal point (b). (Kyle Simek, Creative Commons license. http://ksimek.github.io/pinhole_camera_diagram/, accessed June 2017).*
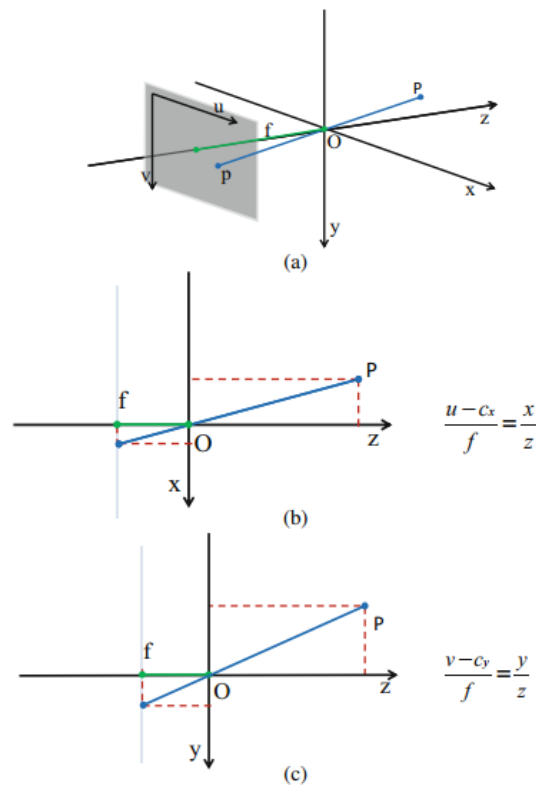
$$\frac{u - c_x}{f} = \frac{x}{z}$$

$$\frac{v - c_y}{f} = \frac{y}{z}$$

Figure 2.5 – *Perspective projection geometry. (a) 3D scene – (b) horizontal section of (a) – (c) vertical section of (a) (Zanuttigh et al., 2016).*

$$\begin{cases} u - c_x = f\frac{x}{z} \\ v - c_y = f\frac{y}{z} \end{cases} \tag{2.1}$$

where: u = Horizontal pixel coordinate [px]

v = Vertical pixel coordinate [px]

c_x = Horizontal coordinate of principal point [px]

c_y = Vertical coordinate of principal point [px]

f = Focal length [mm]

x = Horizontal point coordinate [mm]

y = Vertical point coordinate [mm]

z = Distance between sensor plane and point [mm]

The projection from 2D camera coordinates to 3D real-world units is ruled by a non-linear relationship presented in Equation 2.2, in which the 3 by 3 matrix is commonly called the *camera matrix*, *intrinsic parameters matrix* or *projection matrix*. Axis skew is theoretically present in this matrix but is often neglected in practice and will not be presented here.

$$z \begin{bmatrix} u \\ v \\ 1 \end{bmatrix} = \begin{bmatrix} f & 0 & c_x \\ 0 & f & c_y \\ 0 & 0 & 1 \end{bmatrix} \begin{bmatrix} x \\ y \\ z \end{bmatrix} \tag{2.2}$$

Finally, in real imaging systems, the use of lenses distorts the coordinates of points on the sensor. Correct pixel coordinates can be computed on the basis of the measured pixel coordinates and the characteristics of the lens by inverting distortion models (Equation 2.3). A real camera presents radial and tangential distortion. Tangential distortion is often deemed negligible when compared to radial distortion and is not considered in this study.

$$p = \Psi^{-1}(\hat{p}) \tag{2.3}$$

where: p = Undistorted pixel coordinates [px]

$\hat{p}$ = Distorted pixel coordinates [px]

Ψ = Distortion model

All parameters presented in this section can be estimated by the means of a geometric calibration, following various methodologies such as that proposed by Zhang (2002) based on the acquisition of checkerboard images, where the camera parameters are estimated via detection of a pattern of known size. This technique was used and is developed in section 3.4.2.

2.4 Active triangulation

The active triangulation working principle is central to this study, as the SR300 camera relied on it to capture 3D frames of the basil plants. Cameras based on active triangulation

are commonly called *structured light depth cameras*, because depth (i.e. distance between camera plane and object) measurements are based on the projection of a structured light pattern. The *active* adjective reflects the presence of a *projector* or *illuminator* in the design of the sensor and marks the difference between such devices and passive triangulation devices such as stereo depth cameras.

The principle of optical triangulation is represented in the diagram of Figure 2.6. Point coordinates are computed by trigonometry as explained by Blais, Rioux, and Beraldin (1988) (Equations 2.4 and 2.5).

$$Z = \frac{d\,l'}{p + l'\,\tan\theta}$$
$$X = Z\tan\theta \tag{2.4}$$

where: p = Point coordinate on the sensor [px]
X = Point coordinate in the scene [mm]
Z = Camera-point distance [mm]
θ = Deflection angle of the laser beam [°]
d = Baseline (distance between light source and lens) [mm]

and l' is given by Equation 2.5 :

$$l' = \frac{l\,f}{l - f} \simeq f \tag{2.5}$$

where: l' = Distance between the sensor and the lens
l = Distance between the sensor and the object plane
f = Focal length of the lens

The previous approximation holds if $l \gg f$.
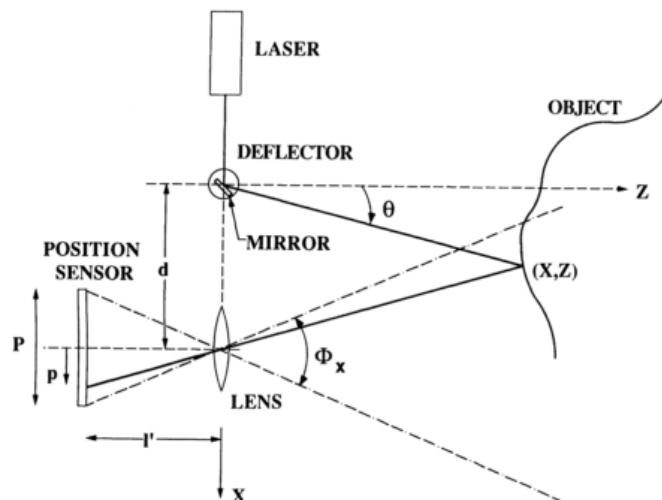
Figure 2.6 – *Active triangulation diagram comprising a sensor, a laser and a deflector (Blais et al., 1988).*

The projector illuminates the scene with a structured light pattern coded in binary words. Correspondence between the projected pattern and it's measured counterpart is estimated to determine on which points the triangulation can be computed. Indeed, the structured light approach faces a limitation in the form of shadow effect, illustrated in Figure 2.7 and due to the geometry of such devices. Some points are not illuminated, while others are illuminated but not detected by the camera. When a correspondence exists between points, they are called conjugates and the coordinates of said conjugate points in the scene are computed by triangulation.
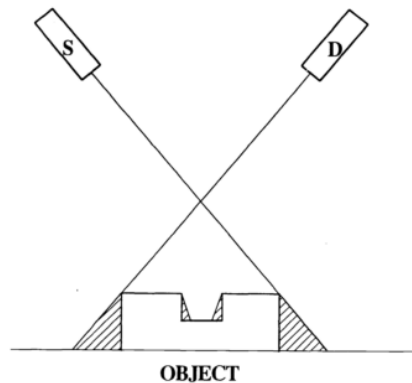
Figure 2.7 – *Shadow effect due to the nature of optical triangulation. Some regions cannot be detected because of occlusion from the perspective of either the light source (S) or the detector (D) (Blais et al., 1988).*

2.5 4D reconstruction

Four dimensional reconstruction of plants is a complex technique based on three dimensional measurements taken at regular time intervals.

Three dimensional measurements, for example taken by a red-green-blue-depth (RGB-D) camera, can be represented as 3D point clouds. The data type stores points coordinates (X, Y, Z), and if provided, maps texture to them. Point clouds come in various sizes, encompassing a single plant in the present case, or large items or rooms in robotics related applications (Figure 2.8).
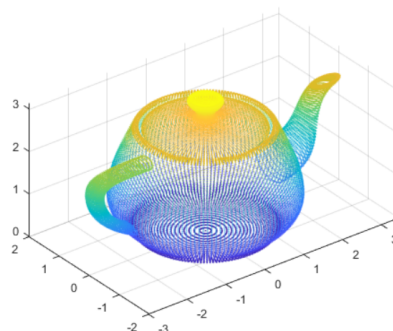
Figure 2.8 – *Point cloud of a tea pot from the Matlab Computer Vision Toolbox examples data set.*

A very interesting trend in plant phenotyping is the addition of the time axis to those 3D measurements, hence the term "4D reconstruction". The huge challenge in plant 4D reconstruction lies in the dynamic nature of shapes (Dong et al., 2016). Y. Li et al. (2013) present a multi-labeling technique : an approach where each stem and each leaf is segmented and well identified, with correspondence of organs over time. They proposed a technique to monitor the growth of various plants over time with the help of precise point clouds, implementing a forward-backward approach for event detection : their algorithm would analyze data over time, and when an event such as budding was detected with high certainty, a backward analysis was initiated to find the precise moment of event occurrence (Figure 2.9).
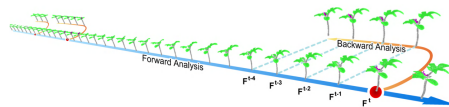
Figure 2.9 – *Forward backward analysis pipeline used by Y. Li et al. (2013). An event is detected with high certainty in F^t in the forward analysis. A backward analysis is initiated to find the exact time of the event occurrence.*

Paproki et al. (2012) established a phenotyping technique that uses multiple 3D views to reconstruct complete point clouds, segment plant organs and estimate topological characteristics of *Gossypium hirsutum L.*

In the field, Dong et al. (2016) recently developed a method of spatio-temporal reconstruction for 4D crop monitoring (Figure 2.10), based on structure from motion stereoscopic images, a 9 degrees of freedom inertial measurement unit and an RTK-GPS positioning system[1].
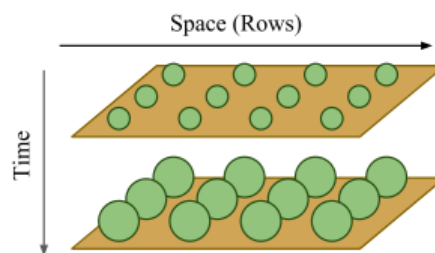
Figure 2.10 – *4D reconstruction model, with the time axis added to three dimensional space (Dong et al., 2016).*

---

[1]RTK-GPS is a positioning system providing great accuracy, used in precision agriculture applications.

Chapter 3

Materials and Methods

This chapter details the conditions of the experiment, during which basil was cultivated in a controlled environment with hydroponic system and monitored by the means of an automated 3D image acquisition device (Figure 3.1).
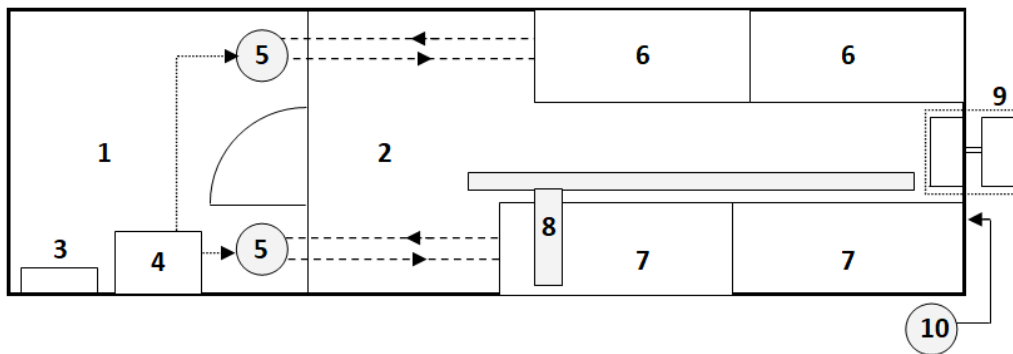
Figure 3.1 – *Non scaled schematic of the container. 1 : equipment room - 2 : growth chamber - 3 : electrical panel - 4 : pH-up and water injection set-up - 5 : water tanks (2) - 6 : separate experimentation - 7 : basil hydroponic system - 8 : RGB-D camera secured on the displacement rail - 9 : air conditioning - 10 : CO_2 tank. Dashed lines : nutrient solution flow - dotted lines : pH-up and fresh water injection pipes - full line : CO_2 injection pipe (Courtesy of B. Stalport).*

3.1 Plant material

3.1.1 Basil

Basil (Ocimum basilicum L.) was chosen for this study because of it's simple architecture, and it is a common product of indoor agriculture.

First of all, as a member of the Lamiaceae family, basil displays a relatively simple architecture with decussate leaves. The assumption was made that this trait would limit optical occlusion between leaves borne by successive internodes when the plant is seen in nadir view[1]. Axillary shoots may arise in late growth stages, but were not a primary concern in this research.

---

[1]The nadir is defined as the orientation that is vertical and pointing in the direction of the force of gravity at a given point. This term is more precise than "top view" or "from above" (Wikipedia, 2017)

Finally, cultivating basil in controlled conditions is deemed a viable economical endeavor by Liaros, Botsis, and Xydis (2016). Indeed, the study concluded that small urban indoor plant factories can constitute an asset for local retail market, provided that the produced plants present high added value, which is the case for medicinal plants and, in the present case, herbs. It is also one of the products cultivated by an industrial partner of the Precision Agriculture laboratory. Conducting a research on this plant allowed us to make several tests and observations that may prove useful in the future of that partnership.

Sowing took place on May 23, 2017. The 12 plants were in a germination area until June 12, when they were relocated to the growth chamber. Durations are expressed in days after sowing (DAS) in the rest of this report.

3.1.2 Direct measurements

During the experiment, a series of parameters (Figure 3.2) were measured on half of the plants — i.e. on six individuals — to serve as ground truth topology, at four different time points. Measurements were carried out with the help of a digital vernier caliper with a rated accuracy of 0.02 mm. However, in this particular situation, the characteristics of the instrument become irrelevant as the measurement uncertainty majorly comes from the difficulty for the operator to access plants because of their neighbors. The parameters were chosen to best describe the topological traits of interest in the frame of this work, i.e. organs dimensions and appearance, while being fairly easy to measure or estimate. The list of measured parameters comprised :

- internode height (h_i) ;
- projected leaf length (L_{ij}) ;
- leaf width (w_{ij}) ;
- projected petiole length (P_{ij}) ;
- insertion angle of petiole on the stem, estimated on a discontinuous scale of 15° steps (θ_{ij}) ;
- height difference between petiole tip and leaf tip (Δh_{ij}) ;
- leaf curvature (qualitative classification in 4 classes based on the orientation and intensity of the curvature) ;
- leaf texture (smooth or rough).

Indices are relative to plant internodes : $i = \{1, 2, \ldots, n\}$ with the first being the lowest one, i.e. between the substrate surface and the first node, and n the number of internodes, and leaves borne by said internodes : $j = \{1, 2\}$. Based on those simple measurements, other parameters could be computed, such as :

- the main stem height as the sum of internodes heights ($H_{stem} = \sum\limits_{i=1}^{n} h_i$) ;
- the total plant height as the highest Δh added to the main stem height ($H_{tot} = H_{stem} + \Delta h_n$) ;

- the real plant length by the Pythagorean theorem ($L_{r,ij} = \sqrt{L_{ij}^2 + \Delta h_{ij}^2}$), considering the real length as the hypotenuse of a right triangle (Figure 3.2b).

(a) *Plant measurements.*
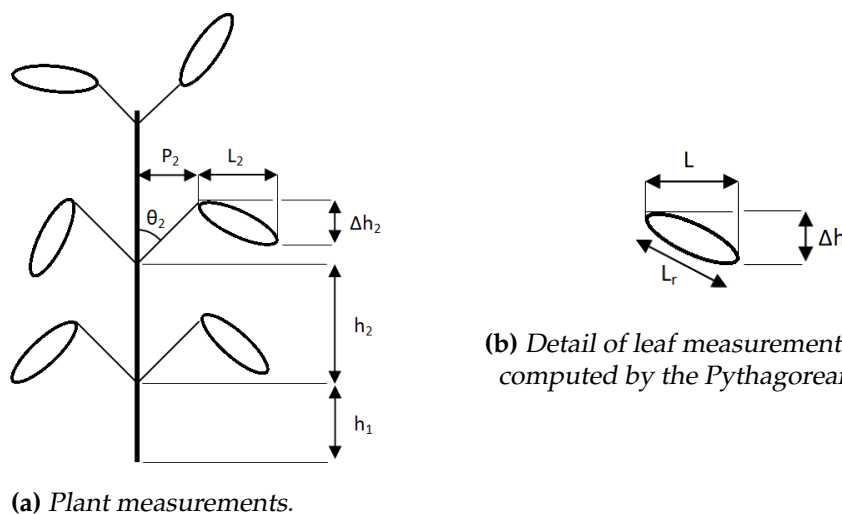
(b) *Detail of leaf measurements. L_r can be computed by the Pythagorean theorem.*

Figure 3.2 – *Diagram of direct measurements that were taken on 6 plants at 4 time points. P : projected petiole length ; L : Projected leaf length ; θ : insertion angle of petiole on the stem ; Δh : height difference between the tip of the petiole and the tip of the leaf ; h : internode height.*

3.2 Data acquisition and regulation equipment

Data logging relied on the use of two separate Campbell Scientific CR1000 dataloggers : one for nutrient solution measurements and the second for climate-control related measurements. All measurements were transferred onto an online server.

Two single board computers were used for this experiment : a Raspberry Pi and an Up Board. On one hand, the Raspberry Pi commanded a custom printed circuit board (PCB) and handled the hydroponic regulation systems brought up in the next section, based on the measurements sent to the server by the CR1000 data loggers. On the other hand, the Up Board was in charge of driving the light-emitting diode (LED) lighting system and capturing the RGB and depth images. The choice of the Up Board relied on the advertised partnership between it's manufacturer, AAEON Technologies, and Intel Corp., manufacturer of the image acquisition device used in the study (Intel RealSense SR300 RGB-D camera) which ensured compatibility between both devices.

3.3 Growth conditions

3.3.1 Growth chamber

The growth chamber was located in a 20 ft Reefer container. The most interesting characteristics of this device are it's efficient insulation, airtightness and its integrated heating, ventilation and air-conditioning (HVAC) system.

However, an external air-conditioning unit was used to regulate the temperature inside the growth chamber for energy efficiency concerns. The temperature set point was 21 °C

during the day (6 a.m. to midnight) and 18 °C during the night (midnight to 6 a.m.). This temperature range was decided in consultation with scientific collaborators and had to accommodate an other experiment taking place inside the growth chamber simultaneously, where lettuce was grown in an aquaponic system.

To ensure that temperature regulation was based on representative data, three temperature probes were placed inside the growth chamber. The air-conditioning unit would turn on when the mean of the three measurements went above the set-point. The integrated ventilation system provided air mixing and temperature homogenization inside the air conditioned enclosure.

To provide CO_2 fertilization, concentration in the growth chamber was kept at high levels throughout the experiment : the set-point was 1000 ppm. As can be seen on Figure 3.3, CO_2 levels were quite inconsistent throughout the experiment. Concentration drops were due to the opening of the growth chamber door, while peaks were due to the presence of people, often for measurement purposes. However, by zooming in on a short period of time from day 27 to day 32 , one can have confirmation that the regulation process of CO_2 concentration was effective. Indeed, during this period, the container remained closed most of the time, diminishing disturbances and finally leaving a chance for the regulation process to perform better. Finally, despite the large variations of CO_2 levels attested by a coefficient of variation of 24 %, concentration levels remained above the set-point 62% of the time.
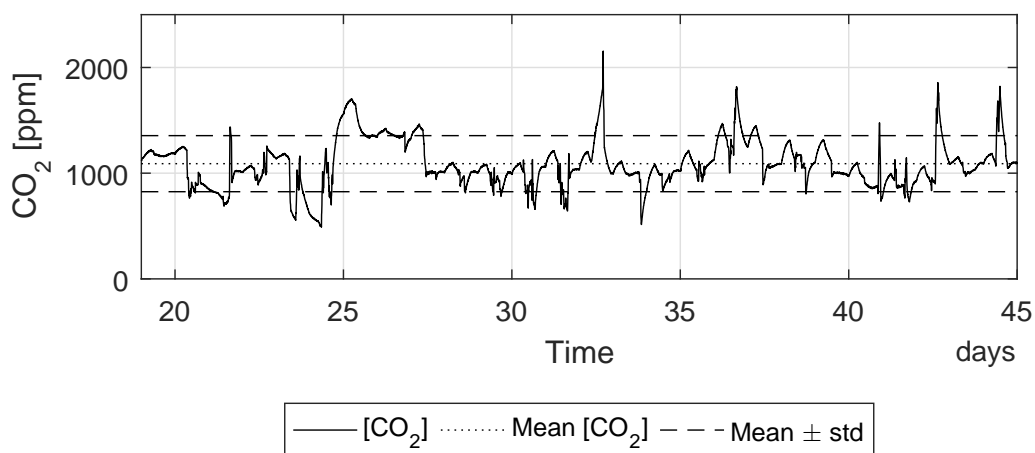
Figure 3.3 – *CO_2 concentration throughout the experiment.*

3.3.2 Hydroponic system

Two dark plastic polypropylene containers of 30 L were used as study tanks, with an additional 50 L opaque tank in the equipment room containing hydroponic solution related probes while being easily accessible for measurements and interventions without disturbing the growth of the basil plants inside the growth chamber. The total liquid volume was 50 L, as the containers were only partially filled. A 144 W membrane pump provided water influx to both containers, connected in a parallel circuit with a volume flow rate of 8 L·min^{-1}. The return to the main tank occurred through an overflow in adjustable pipes. This setup ensured efficient water flow and thus solution homogenization in the

whole set-up, essential for representative measurements and pH regulation.

(a) *Peat pellet.*

(b) *Pots containing wet, expanded peat pellets.*

Figure 3.4 – *Peat pellets used during the experiment. (a) Dry, compact peat pellet. (b) Wet, expanded peat pellets.*

Peat pellets were used as substrate because of their satisfying quality/cost ratio. On the two 30 L containers sat four extruded polystyrene foam (XPS) lids, each pierced of 23 holes allowing the placement of net pots that kept the substrate partially submerged. Figure 3.4 pictures the substrate and Figure 3.5 shows the set-up of the containers and XPS lids. For future reference, those XPS lids constitute the ground level of the experimental set-up.
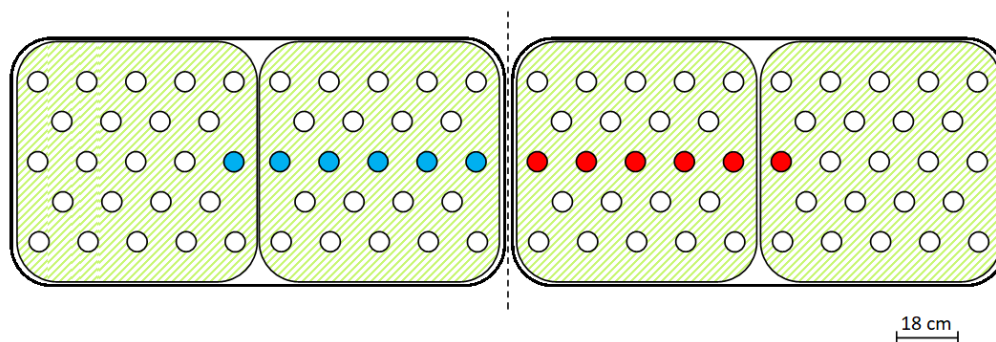
Figure 3.5 – *Layout of the two 10 L containers with the XPS lids (green). Colored spots mean the hole is occupied by a plant, with colors indicating the light recipes. The dashed line separates the area in two. White holes were either empty and covered or containing backup plants.*

The difference in hole colors in Figure 3.5 actually symbolizes the light treatment. To bring light to the plants, an array of 224 LED lights was assembled, comprising 128 white LEDs, 64 red LEDs and 32 blue LEDs, symmetrically placed on two sub-arrays. The LEDs were linked in series circuits of 8 for the red and the white ones, and in series circuits of 4 for the blue ones, totaling 32 different channels. Figure 3.6 displays the LED array, where numbers represent the various channels and the white channels go by pairs of columns, labeled in the bottom of the image (W_1, W_2, ... , W_{16}). These were powered by an *eldoLED POWERdrive 6060/R* power supply, capable of delivering a maximum power of 600 W. The current intensity delivered to the channels was set to 750 mA. Channels were independently dimmed by a digital multiplexer (DMX), allowing to easily set the intensity of each channel on an 8-bit scale (0-255), with the full scale value of 255 corresponding to the maximum intensity of 750 mA. A Python script (Appendix A) was developed to establish serial communication between the UP Board and the DMX.

To ensure diversity in topological phenotypes appearing in the experiment, the basil
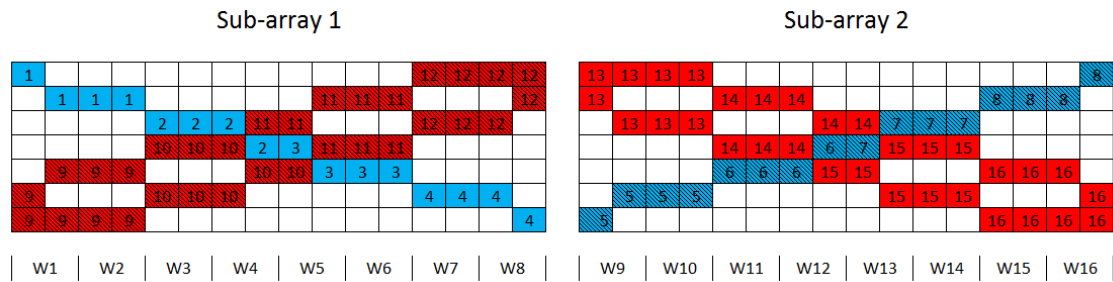
Figure 3.6 – *LED array layout seen from above. Numbers represent blue and red channels, while white channels are numbered in the bottom in the form W_1, W_2, ... , W_{16}. Shaded squares represent the channels that were turned off during the experiment.*

plants were separated by an opaque plate in two groups of different light recipes. One with blue LEDs on and red LEDs off, and the second with blue LEDs off and red LEDs on. The difference between groups lay in light spectrum distribution and not in total energy delivered. Indeed, the photosynthetic photon flux density (PPFD) was set to values of roughly $70\,\mu mol \cdot m^{-2} \cdot s^{-1}$ under both sub-arrays at the level of the XPS lids (i.e. $70\,cm$ below the lamps), which was achieved thanks to the high modularity of the installation. Measurements were taken with the photosynthetically active radiation (PAR) sensitive probe of a *Delta Ohm HD 2102.2* photoradiometer. According to Folta and Childers (2008), such light treatments would give way to different phenotypes in terms of biomass, internode lengths and leaf size. This phenomenon had also been previously observed by scientific collaborators (Blanchy, Hubert, Lahaye, Maron, & Taguem, 2014). To maximize light efficiency and mitigate border effect, the enclosure of the basil plants was made of reflective fabric, with spaces between the different pieces to ensure airflow and prevent excessive humidity accumulation.

Regarding the hydroponic nutrient solution, the two parameters of interest were pH and electrical conductivity (EC), which are main concerns for the proper growth of plants in hydroponic systems (Kozai, 2016). They were continuously measured throughout the experiment by the means of dedicated pH and conductivity probes, and data was logged by a Campbell Scientific CR1000 data logger. Complementary measurements were taken five days a week with a Hach Q40D Multimeter probe, to serve as reference values and possibly to recalibrate the sensors continuously measuring solution parameters.

The set-point for pH regulation was 6 to ensure proper nutrient absorption by the roots (Kozai, 2016). Experienced collaborators mentioned that, in the usual growth conditions that were met in the growth chamber, pH tended to acidification. Knowing that, $5\,L$ of KOH 0.5% pH-up solution were prepared for pH regulation. Figure 3.7 shows the evolution of pH throughout the experiment and mainly confirms this downward trend, except at the beginning of the growth cycle and towards the end. An issue occurred between days 27 to 31, where pH plummeted below the set-point. This problem was due to the intervention of maintenance staff around the regulation circuit board, which lead to a poor contact that took some time to detect. After the diagnosis, measures were taken and regulation resumed.

Basification started again on day 38 until the end of the experiment. This shows that

for future experiments, a pH-down solution should also be available in order to fully control the pH of the nutrient solution.
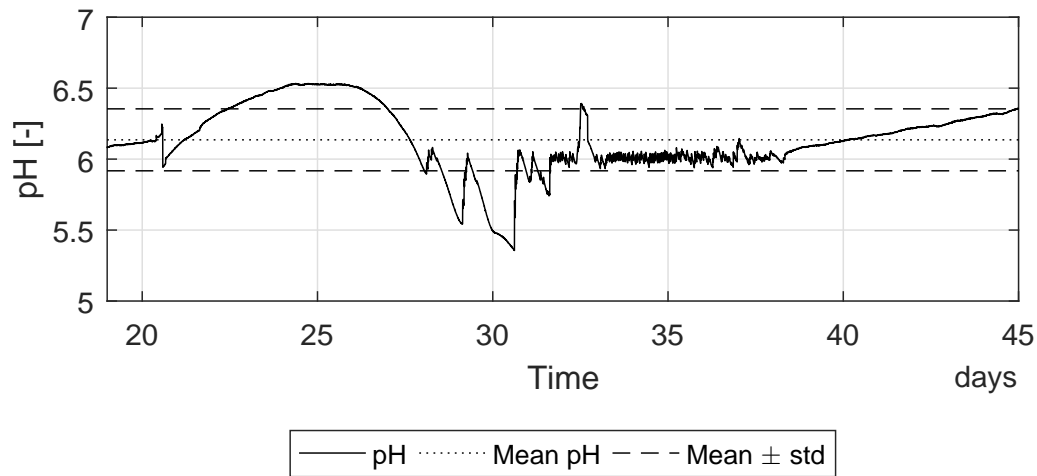
Figure 3.7 – *pH levels throughout the experiment.*

EC informs on the salt concentration in the solution and therefore gives an indication of the nutrients available to the plants. For herbs such as basil, appropriate levels range from $1.4\,\text{dS·m}^{-1}$ to $2.2\,\text{dS·m}^{-1}$. For the purpose of this experiment, EC was set to $1.5\,\text{dS·m}^{-1}$ with Aptus All-In-One Liquid Fertilizer (NPK : 3-9-5 % in mass) at the beginning of the experiment and no extra fertilizer was added afterwards.

3.4   Image acquisition and treatment

3.4.1   RGB-D camera

RGB-D stands for **R**ed **G**reen **B**lue–**D**epth. As the name suggests, an RGB-D sensor captures color frames in the form of RGB pictures, and depth frames that contain distance information. The sensor central to this study was the Intel RealSense SR300 RGB-D camera (Figure 3.8), a consumer-grade product designed for computer gaming and entertainment (e.g. : hands-free computer control). The device shows promise as a low-cost 3D scanner at a time where some studies explore the use of similar structured light depth sensors such as Microsoft Kinect (Azzari et al., 2013; Paulus, Behmann, et al., 2014) for applications in plant phenotyping.

Figure 3.8 – *Intel RealSense SR300.*

Figure 3.9 shows the component locations in the SR300 camera. The imaging application specific integrated circuit (ASIC) processes data before sending it to the USB3-connected client system (i.e. a computer).
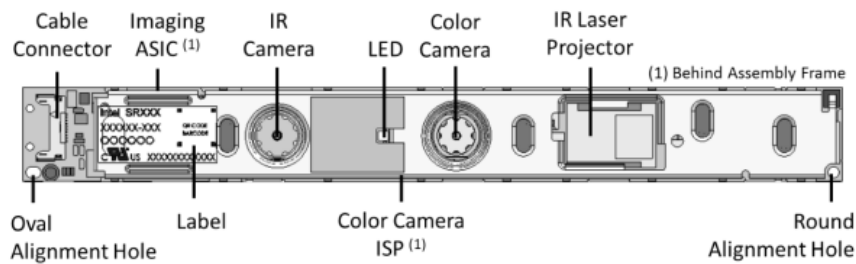
Figure 3.9 – *SR300 components locations (SR300 datasheet).*

The SR300 provides 3 types of output : RGB images, infrared (IR) images and depth images.

RGB images are captured by a chromatic sensor — whose exact type is undisclosed — and processed by the integrated image signal processor, then the imaging ASIC and finally transmitted to the client system (i.e. connected computer).

As for IR images, the camera possesses an IR projector which illuminates the scene with a white pattern (i.e. a uniform intensity). The pattern is reflected by the scene and captured by the IR camera. Pixel values are processed by the imaging ASIC and transmitted to the client system.

Finally, the working principle on which depth images capture relies on is active triangulation, or structured light (section 2.4). It relies on infrared pattern projection and capture of the reflected pattern by the IR camera.

The actual detailed procedure by which depth data is acquired by the SR300 is not publicly available, as it is the intellectual property of the manufacturer. However, the SR300 datasheet gives the following piece of information about depth images acquisition : "*the IR (infrared) projector illuminates the scene with a set of increasing spatial frequency coded vertical bar patterns. These patterns are warped by the scene, reflected back and captured by the IR camera. The IR camera pixel values are then processed by the imaging ASIC to generate a depth frame*", pointing at spatial multiplexing (Zanuttigh et al., 2016).

The recent study by Carfagni et al. (2017) adds some details relative to pattern projection. The IR projector is actually made of three components : an IR laser, a line lens and a resonant micro mirror. The line lens turns the IR laser point into a line, which is projected by the rapidly moving mirror onto the scene. The camera then detects the reflected pattern that is emitted back by the scene and acquires the depth frame.

Table 3.1 shows infrared and color camera properties and Table 3.2 shows the infrared projector properties, essential for proper acquisition set-up geometry design.

Finally, image acquisition used the existing `cpp-headless` software from the open source library LibRealSense (2017). It captured the last RGB and depth frame out of a series of 30 frames to ensure camera parameters stabilization, much like Carfagni et al. (2017) did in their experiment. Its name "headless" reflects the fact that the program

comes without graphical user interface : calling the executable only prints said frames to the current working directory.

Table 3.1 – *Infrared and color camera properties (SR300 datasheet).*

	Infrared camera (depth)	Color camera
Active pixels	640 x 480	1920 x 1080
Aspect ratio	4:3	16:9
Vertical field of view [°]	55 ± 2	41.5 ± 2
Horizontal field of view [°]	71.5 ± 2	68 ± 2
Diagonal field of view [°]	88 ± 3	75.2 ± 4
Inclination	± 1° yaw/pitch tilt	± 1° yaw/pitch tilt
Range [mm]	200 - 1200	

Table 3.2 – *Infrared projector properties (SR300 datasheet).*

	Description
Projector	Coded light
Laser wavelength [nm]	860
Laser compliance	Class 1, IEC 60825-1:2014 Ed 3
Vertical field of projection [°]	60 ± 4
Horizontal field of projection [°]	72.5 ± 2
Inclination	5 ± 2 ° yaw tilt towards IR camera

3.4.2 Intrinsic camera parameters

To estimate intrinsic parameters of the camera (section 2.3), a checkerboard calibrations of both IR and RGB cameras were realized with the Single Camera Calibration App (Computer Vision System Toolbox, MATLAB R2016a, The MathWorks Inc., Natick, MA), which is a user-friendly implementation of the Zhang (2002) method. Only the IR camera calibration is presented here.

The data set used for calibration comprised 30 frames of a flat checkerboard pattern of known square size (40 mm), in a distance range resembling the distance between the camera and the objects of interest. A distance ranging from 500 to 600 mm was chosen to remain consistent with the measurements taken in the hydroponic system. Many pictures were taken to fill most of the image frame. This was necessary to have a good grasp of the radial distortion, which increases with respect to the distance from the center of the image.

The calibration algorithm first detected intersection points of the checkerboard pattern on all images (Figure 3.10), then computed the camera's intrinsic parameters. Results of the calibration were analyzed to ensure proper algorithm execution, especially regarding radial distortion (Figure 3.11). Camera parameters are presented in Table 3.3.

Based on the definition of Kalantar-zadeh (2013), depth resolution (also called discrimination) is the smallest depth difference that the camera is able to detect. It was computed by Equation 3.1 (Blais et al., 1988) and plotted in Figure 3.12. Focal length was obtained
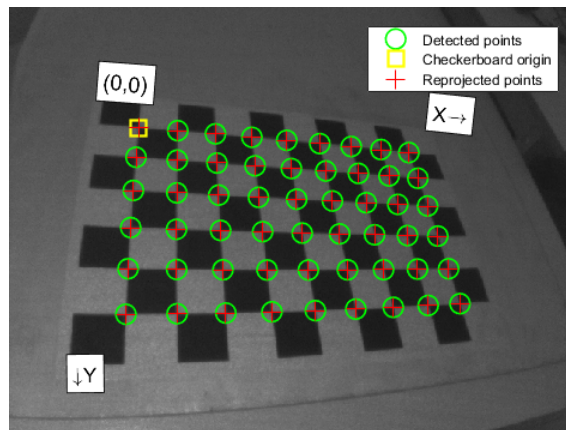
Figure 3.10 – *Checkerboard calibration of the IR sensor. The calibration algorithm detects pattern intersections and extracts camera parameters based on the known dimensions of the pattern's squares.*
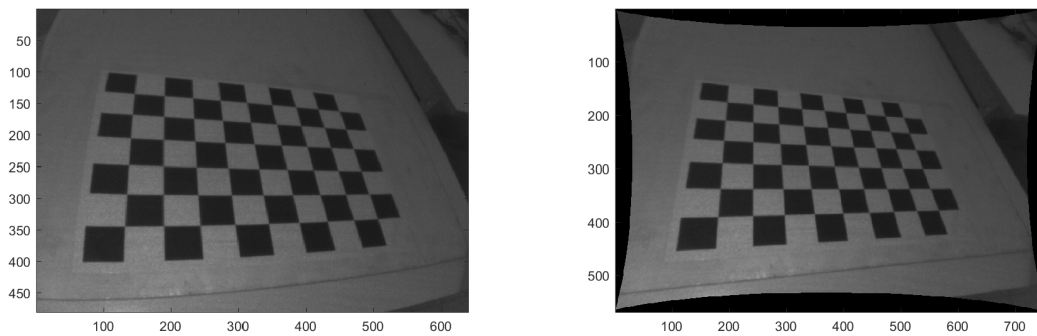
(a) *Original, distorted IR image.*

(b) *Undistorted IR image.*

Figure 3.11 – *IR images of checkerboard pattern used for camera calibration.*

Table 3.3 – *Camera intrinsic parameters and lens distortion extracted from checkerboard calibration.*

Parameter	Value	Standard deviation	Unit
Focal length X	478.9433	0.3964	px
Focal length Y	477.0327	0.3851	px
Principal point X	315.7035	0.3531	px
Principal point Y	238.1820	0.5091	px
Radial distortion X	-0.1309	0.0018	-
Radial distortion Y	-0.0259	0.0051	-
Mean reprojection error	0.02054	-	px

through checkerboard calibration (Table 3.3), while baseline and disparity resolution are provided in the datasheet. According to Guidi, Gonizzi, and Micoli (2016), the disparity resolution corresponds to the error on the measurement of the position of dots in the projected pattern and is affected by the IR camera noise.

$$\Delta z = \frac{z^2}{b \cdot f} \cdot \Delta d = \frac{z^2}{48 \cdot 478.9701} \cdot \frac{1}{8} \tag{3.1}$$

where: Δz = Depth resolution [mm]

z = Depth [mm]

b = Baseline [mm]

f = Focal length [px]

Δd = Disparity resolution [px]
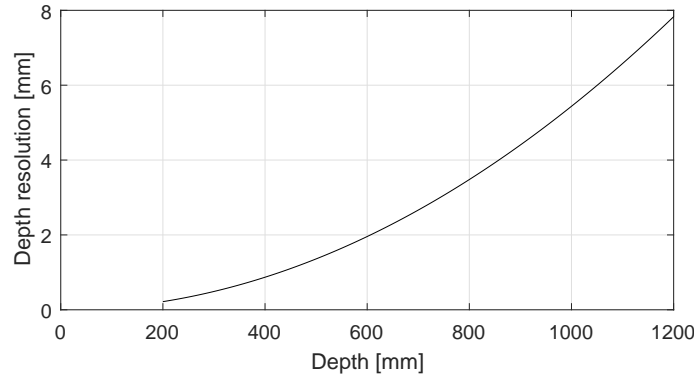
Figure 3.12 – *Depth resolution with respect to depth, within the range prescribed by the manufacturer for the SR300.*

3.4.3 Depth data calibration

3D information was provided as depth, i.e. the distance between the scanned object and the camera. Depth data was encoded on the three channels of a portable network graphics (PNG) file with a resolution of 16 bits, in a RGB565 bitmap format : 5 bits were stored in the red channel, 6 bits in the green channel and 5 in the blue channel. Each channel contained distance information at different scales, with the most significant bit stored in the red channel and the least significant bit in the blue one, which meant that the depth map had to undergo a conversion operation to express a continuous distance scale (Equation 3.2).

$$Sc = 2^{11} \cdot R + 2^6 \cdot G + 2^0 \cdot B \tag{3.2}$$

where: Sc = Scaled depth value [distance unit]

R = Red pixel intensity [-]

G = Green pixel intensity [-]

B = Blue pixel intensity [-]

Given Equation 3.2, it becomes clear that :

- a value of 1 stored in the blue channel equates $2^0 = 1$ unit of distance ;
- a value of 1 stored in the blue channel equates $2^6 = 64$ units of distance ;
- a value of 1 stored in the blue channel equates $2^{11} = 2048$ units of distance.

Figure 3.13 shows the same image, before and after scaling. The scaled image is displayed through the `imagesc` function.
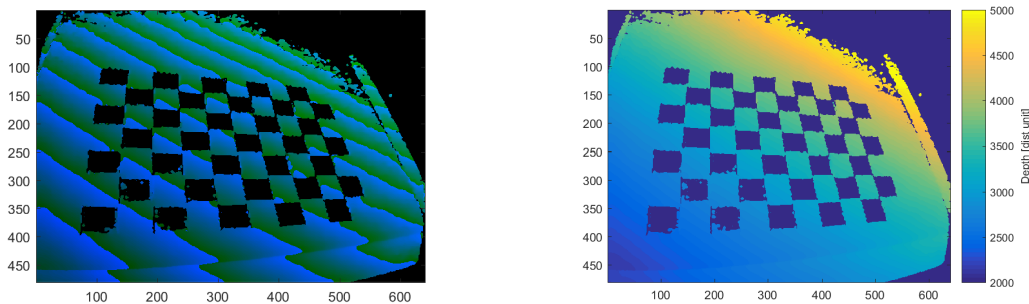
(a) *Checkerboard image before scaling.*   (b) *Scaled checkerboard image.*

Figure 3.13 – *Checkerboard depth map, (a) before and (b) after scaling.*

The final step of calibration was to convert the arbitrary depth units to real world units. To achieve this, pictures of a flat surface were taken at several distances to compute a calibration curve. Both the camera and the flat surface were secured to 30 mm Bosch profile mounts. To achieve parallelism, a Bosch DLE 70 laser meter was used to measure the distance between the front face of the camera and the plane surface at two opposite points. It's advertised accuracy is 1.5 mm. The pixels used to establish the calibration curve were in a central square of 200 by 200 pixels. Indeed, Carfagni et al. (2017) suggest that for such a sensor, the edges of the framed areas are prone to strong deformations and depth pixel values can become aberrant. The value retained as calibration data was the mean of the values contained in that central square . The resulting relation is plotted in Figure 3.14. This simplification was possible because the acquisition set-up was designed to take pictures in nadir view, with images centered on the plant of interest.

Table 3.4, from the paper of Carfagni et al. (2017), presents interesting image characteristics. The scale factor is computed by Equation 3.3. It is function of the following geometric parameters, represented in Figure 3.15 (courtesy of F. Uccheddu, coauthor of Carfagni et al. (2017) via e-mail exchange) : half of the field of view (FOV) opening angle β (horizontal : 71.5 °or vertical : 55 °) ; the half width (320 px) or the half height (240 px) and the distance between the camera and the framed object. In simple terms, the scale factor is the ratio between real-world image height and width in millimeters to image height and width in pixels (respectively 480 and 640 px). It increases linearly with distance.
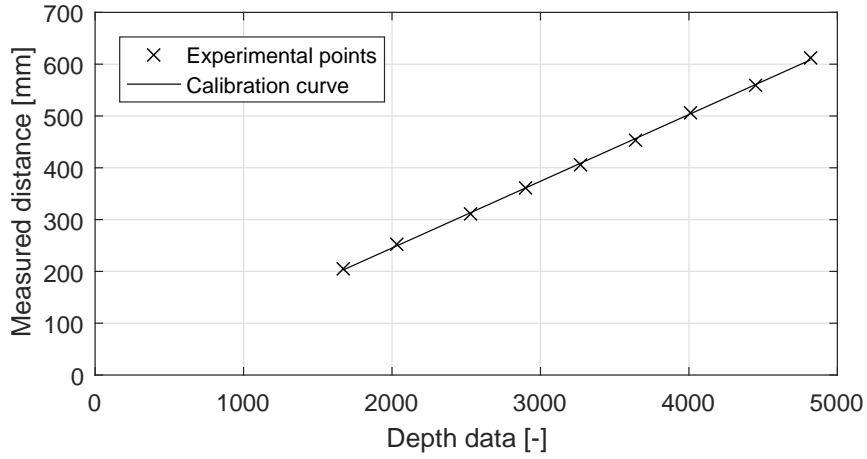
Figure 3.14 – *Depth linear calibration curve.*
$$D_{mm} = 0.1286 \times D_{data} - 12.61$$
$$R^2 = 0.9996 \; ; RMSE = 2.64 \, \text{mm}$$

Table 3.4 – *Geometrical image characteristics of SR300 IR and depth camera (Carfagni et al., 2017). X and Y stand for real-world image width and height, respectively.*

Distance	X	Y	Scale factor	Framed area	Point density
$[mm]$	$[mm]$	$[mm]$	$[mm.px^{-1}]$	$[mm^2]$	$[points.mm^{-2}]$
200	256	192	0.4	49152	6.25
450	640	480	1	307200	1.00
600	832	624	1.3	519168	0.59
800	1152	864	1.8	995328	0.31
1000	1472	1104	2.3	1625088	0.19

$$SF = \frac{\tan \beta}{x} \cdot d \qquad (3.3)$$

where: SF = Scale factor [mm/px]

β = Half FOV angle (H : 35.75 °; V : 27.5 °) [°]

x = Half of image width (320 px) or height (240 px) [px]

d = Camera-object distance [mm]
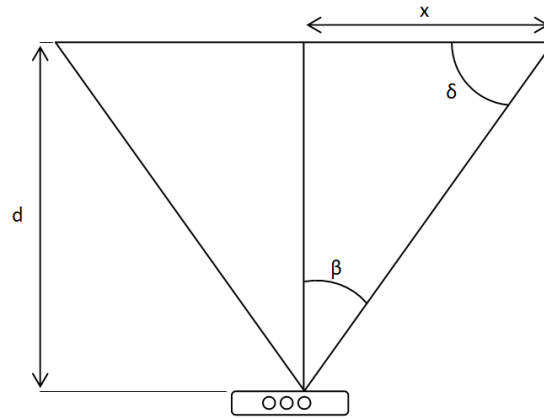
Figure 3.15 – *Diagram of the underlying geometric parameters of Equation 3.3 (Carfagni et al., 2017). d : distance to object [mm] ; x : half of image width or height [px] ; β : half FOV angle ; δ : complement to β.*

The point density can prove itself useful to estimate area of plant organs (mainly leaves) and it's value is ruled by Equation 3.4. It decreases quadratically with distance.

$$PD = \frac{X_0 \cdot Y_0}{FA} = \frac{X_0 \cdot Y_0}{X \cdot Y} = \frac{X_0 \cdot Y_0}{X_0 \cdot Y_0 \, SF^2} = \frac{1}{SF^2} = \left(\frac{x}{\tan \beta}\right)^2 \cdot \frac{1}{d^2} \qquad (3.4)$$

where: PD = Point density [px.mm^{-2}]

X_0 = Image width [px]

Y_0 = Image height [px]

FA = Framed area [mm^2]

X = Real world width of image [mm]

Y = Real world height of image [mm]

SF = Scale factor [mm.px^{-1}]

3.4.4 Image acquisition

The image acquisition set-up was designed to capture nadir view images of the basil plants disposed on the central line of the hydroponic system (Figure 3.5). It is pictured in Figure 3.16.

It comprised a stepper motor linear displacement rail, it's power supply and control circuit, an L-shaped 20 mm Bosch Rexroth profile assembly and a CNC machined foam PVC support for the camera. The camera was secured 530 mm above the the surface of
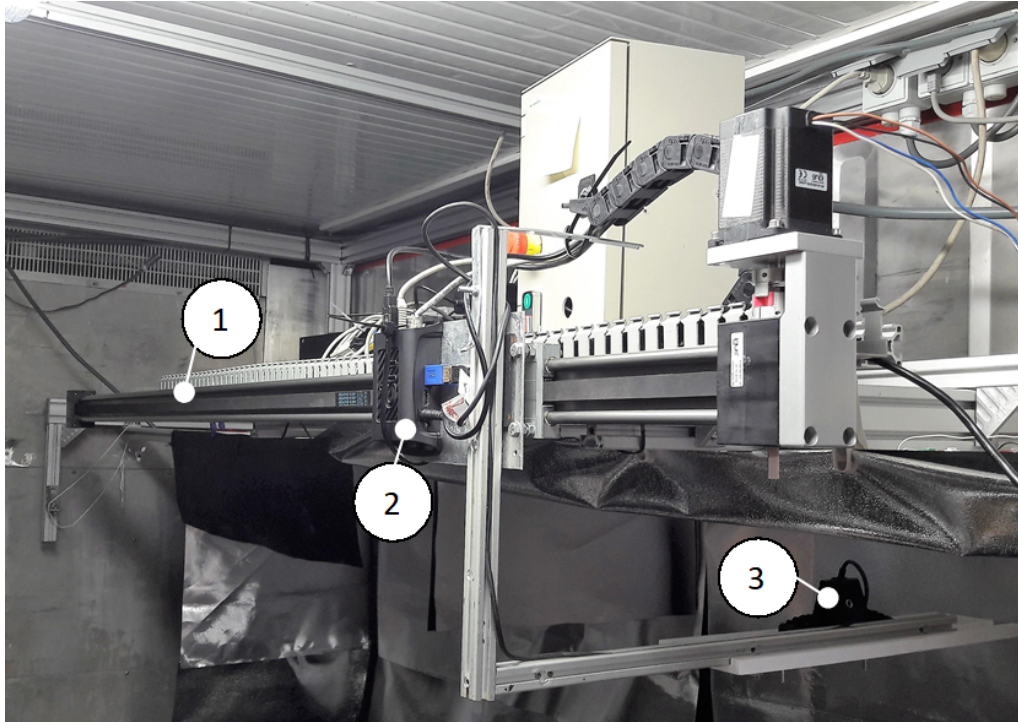
Figure 3.16 – *Image acquisition set-up.*
1 : displacement rail ; 2 : Up Board secured on the displacement rail ; 3 : RGB-D camera.

the XPS lids (i.e. the "ground level") of the hydroponic system to account for the expected plant growth during the experiment, as well as other geometrical constraints. The camera support was designed for easy alignment on the central axis of the XPS lids, where the basil plants of interest were placed. This central position ensured a strict nadir view of the plants.

The Up Board controlled image acquisition by the Intel RealSense SR300, and the displacement rail thanks to an intermediary Arduino microcontroller. The image acquisition program is detailed in the form of a pseudocode (algorithm 1 ; the actual program was coded in C++). At first, all non-white LEDs were turned off to suppress differences in spectrum distribution due to red and blue LEDs. Images were then captured at various positions. A text file containing the relative displacement information was read, and said information was sent via serial communication to the Arduino microcontroller connected to the stepper motor. The camera moved to the first position and a flag was raised when said position was reached. At that moment, RGB and depth pictures were captured by the SR300 camera. Then the acquisition cycle continued to it's next positions, until the last basil plant was reached. At the end of the process, LED lighting returned to it's normal setting and the displacement rail returned in home position.

3.4.5 Image processing

Preprocessing

A mask was manually applied to the images to only leave the plant of interest in each frame, similarly to the method used by Azzari et al. (2013). This was necessary mainly

---

Algorithm 1: Image acquisition program pseudocode.

Data: positions
Result: RGB-D images of each plant
initialization;
turn off red and blue LEDs;
foreach *position in positions* **do**
   move camera **to** position;
   take pictures;
end
turn all LEDs back on;
move camera back home;

---

to remove leaves from adjacent plants that were in contact with the plant of interest, disturbing depth measurement and analysis. To improve computation time, images were cropped to only display the region of interest, i.e. the target plant. They were then scaled following the method explained in section 3.4.3 and converted to height maps. In the case of growing plants, it made sense to convert depth data to height, by subtracting depth to the camera height relative to the surface of the XPS lids, i.e. the "ground level" (Figure 3.17, Equation 3.5).

$$h = H_{camera} - D \qquad\qquad (3.5)$$

where: h = Plant height [mm]
H_{camera} = Camera height [mm]
D = Depth value [mm]
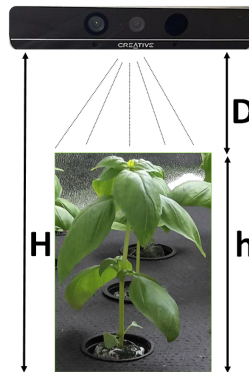
Figure 3.17 – *Height computation diagram. H = distance between camera and ground level ; D = depth of measured point ; h = height of measured point.*

Point cloud conversion and accumulation

Resulting images were then converted to point clouds objects thanks to the pointCloud function of the MATLAB 3-D Point Cloud Processing toolbox. In the process, the background points were removed, thus reducing the quantity of data to be analyzed.

However, a point cloud of a single height map contained the same information but

with a different encoding ; the lower leaves remained hidden by upper leaves. To generate a more thorough point cloud of the plants' topology and manage occlusion issues, the point clouds were accumulated over time. For a given plant, the initial point cloud corresponded to the conversion from height map to point cloud, i.e. the conversion from pixel coordinates to real-world coordinates thanks to the scaling factor computed by Equation 3.3. Height was already present in real-world units in the depth rasters, so only x and y coordinates had to be computed. The real-world reference frame had it's origin located at the coordinates of the optical center of the depth maps, given by the checkerboard calibration (Table 3.3), at ground level. Points coordinates were computed following Equation 3.6. Once the point clouds were generated, a denoising filter was applied to mitigate flying pixel effect (Rusu, Blodow, Marton, Soos, & Beetz, 2007). The flying pixels are artifacts coming from the depth data processing internal to the SR300 camera. Depth is interpolated to generate a larger number of data points than the camera actually measures. To do so, the camera software interpolates between two known points by generating an interpolating function (or interpolant) between these points, thus generating a number of new between measured points. The exact interpolation algorithm remains undisclosed by Intel Corp. The downside of this technique is the presence of flying pixels near depth discontinuities, such as leaves edges. Figure 3.18 showcases flying pixel effect in a transect of a checkerboard image. The black squares do not reflect infrared light, preventing some parts of the projected pattern to be detected by the camera. Hence, they appear to lie at an infinite distance and are set as null values by the camera software, creating a discontinuity in the depth map.

$$(X, Y) = SF(h_{(x,y)}) \cdot (x, y) \tag{3.6}$$

where: (X, Y) = Point coordinates with respect to the optical center of the image [mm]

$SF(h_{(x,y)})$ = Scale factor depending on height at coordinates (x,y) [mm.px^{-1}]

(x, y) = Point coordinates with respect to the conventional axes origin in the top left corner of depth raster [px]

For the following frames of the plant in the time sequence, the same operations were carried out to generate new point clouds. In addition to that, the newly generated points were added to the previous point cloud in order to accumulate information over time (Equation 3.7), thus forming the aforementioned more thorough point cloud. All point clouds were stored at every time step in order to keep a record of the dynamic of the process.

$$PCL_t = \left[pcl_1^{n(1)} pcl_2^{n(2)} \cdots pcl_t^{n(t)} \right] \tag{3.7}$$

where: PCL_t = accumulated point cloud at time t

$pcl_t^{n(t)}$ = point cloud at time t, containing n(t) points

(a) *Checkerboard depth map.*

(b) *Transect of the depth map (a) along the red line.*
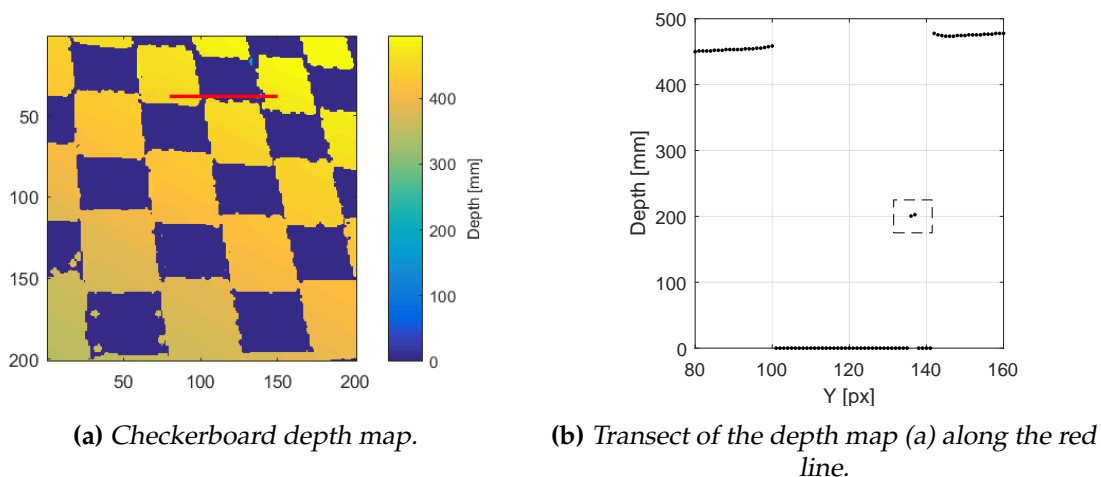
Figure 3.18 – *(a) Depth map of a checkerboard image. Black squares return a depth value of 0, creating depth discontinuities. Flying pixel effect is identified in (b) by the dashed rectangle.*

3.4.6 Feature extraction

The point clouds resulting from this process were analyzed to estimate total plant height over time. Estimations were compared to the direct measurements (subsection 3.1.2) to evaluate the accuracy of the process. To do so, point cloud estimations were plotted against manual measurements. The coefficient of determination was computed, as well as the mean absolute error (MAE, Equation 3.8). According to Willmott and Matsuura (2005), the MAE is a more intuitive way to evaluate error on a model than the widespread root-mean-square error (RMSE) that is more prone to error overestimation.

$$MAE = \frac{1}{n} \sum_{i=1}^{n} e_i \tag{3.8}$$

where: MAE = Mean absolute error
n = Number of observations
e_i = Absolute measurement error

3.5 Harvest measurements

At the end of the growth cycle, final measurements were taken to store as much information as possible about the plants' architecture. First, several side view RGB pictures were taken to have a global representation of each plant. The following measurements consisted of a complete depth scan of the plants, weighing the internodes and measurements of leaves' dimensions.

The RGB side-view pictures were realized with a digital single-lens reflex camera camera. A ruler was placed vertically on the right of the plants to serve as height reference, allowing a rough estimation of the plants' dimensions. This was not intended as a rigorous measurement, since the parallax effect distorts heights readings.

To capture a quasi-complete point cloud of the plant topology, an alternating sequence

of pruning and image acquisition was set in place. The plants' uppermost internode were beheaded between frames, 5 mm above the inferior node (Figure 3.19), thus eliminating all nadir view occlusion for the camera. The architecture was captured by as many snapshots as there were internodes, to provide a clear view of each storey of the plants. All depth frames were converted to point clouds and merged into one point cloud representing the whole architecture. The same denoising filter as in section 3.4.5 was applied, once again to mitigate flying pixel effect. In addition, a merge filter was used to deal with duplicate points : a box grid filter with kernel size 3 was applied to merge points that were close enough to each other so as to be considered duplicates of the same leaf points. This gave birth to a lighter point cloud, without significant loss of topological information.

Figure 3.19 – *Basil plant internodes separated right above each node. During RGB-D acquisition, internodes were removed one after the other with pictures being taken in between, while the plant was still in its spot.*

An analytical balance was set even thanks to the spirit level attached to it and the adjustable feet and used to weigh each internode. The weighing occurred as soon as possible after the plant being cut (within a five minutes range), in order to avoid fresh mass variations due to evaporation.

Finally, all plant material was laid out on custom forms (Appendix B) and glued with transparent sheets of sticking plastic. Once all plants were processed, the forms were scanned in an office scanner (Lexmark MX410de) in tagged image file format (TIFF) with a pixel density of 300 dots per inch (dpi). Measurements were carried out through image analysis. Images were first converted to the hue saturation value (HSV) colorspace and leaves were segmented with Matlab's Image Processing Toolbox Color Thresholder. The `regionprops` function returned the leaves dimensions. The area measurement was trivial as it is computed as the sum of pixels belonging to the segmented region. However, leaves length and width were approximated by the major and minor axes of ellipses presenting the same second-moments as the distribution of the leaves pixels, i.e. the same covariance matrix. This was deemed a more accurate alternative to the bounding box measurements, since this approach would have included petiole length, which was not consistent with the way manual measurements were taken during the experiment. The internodes lengths were measured using the bounding box coordinates, since the length measurement was direct.

To convert the pixel measurements in real-world units, the scale factor was computed

based on the pixel density. The pixel density expressed in dpi informs on the number of points or pixels present on a 1 in, or 25.4 mm line. The computation of the scale factor is then trivial (Equation 3.9).

$$k = \frac{l}{d_{px}} = \frac{25.4}{300} = 84.67 \times 10^{-3} \frac{mm}{px} \tag{3.9}$$

where: k = Scale factor [mm.px^{-1}]
l = 1 in = 25.4 mm long line [mm]
d_{px} = Pixel density [dpi]

The forms were designed with a scaling calibration pattern consisting of four black crosses in the corners of the sheets with their centers at known distances, in millimeters. This allows the conversion to real-world units in the case where pixel density is not known *a priori*. Finally, the correspondence between pixel length or area and real-world units is given by Equation 3.10.

$$L = k \cdot l$$
$$A = k^2 \cdot a \tag{3.10}$$

where: L = Converted length [mm]
l = Measured length [px]
A = Converted area [mm^2]
a = Measured area [px]
k = Scale factor [mm.px^{-1}]

3.6   Topology characterization and graphical representation

As a premise of working with functional-structural plant modeling and phenotyping tools in parallel, the joint use of direct and harvest measurements allowed a graphical representation of basil plants in XPLO software, part of the AMAPstudio suite (Griffon & de Coligny, 2014).

The software handles various file formats, both as inputs and outputs. The preferred input format in this work was the multiscale tree graph (*.mtg files), based on the work of Godin and Caraglio (1998). The MTG format allows easy parameter encoding. The user can even create new classes of components, say a petiole, and assign them appropriate geometrical attributes. In the case of a petiole, the length is an obvious attribute. It is possible to define a wide set of parameters, completely defining plant geometry.

This modularity in plant topology characterization enabled the graphical representation of digital basil plants resembling the real one, based on the manual measurements described in subsection 3.1.2.

Chapter 4

Results and Discussion

4.1   Height measurements

Figure 4.1 shows a bar plot of height over time for the manually measured basil plants (section 3.1.2). Bars are grouped by plant and the shades of grey indicate the various time points. The manually measured ground truth is represented by a square on each bar. The error bars on the estimated (i.e. 3D measured) values are the uncertainty on the measurement and depend on the height of the measured plant : the taller the plant, the smaller the uncertainty. Indeed, uncertainty increases with distance from the sensor, meaning that it will decrease for taller plants which are closer to the sensor (Figure 3.12). The error bars on the ground truth measurements reflect the precision of the measurements taken by the operator in a cluttered environment ; taking measurements on a specimen without disturbing it's neighbors proved itself challenging and most likely generated some error on the measurements.

Figure 4.2 exhibits the comparison between reference values and image-based estimations. Figure 4.2a shows a plot of image measured height versus the reference height. The full line is the first bisector and represents the ideal situation where all estimated points correspond to their reference counterpart, while the dashed line represents the linear model that fits estimated values to the measured reference. Figure 4.2b displays the relative error on the measurements (Equation 4.1).

$$\varepsilon_i = \frac{x_i - X_i}{X_i} \tag{4.1}$$

where: ε_i = Relative error [-]
x_i = Estimated height [mm]
X_i = Reference height [mm]

The first observation that can be made is that the measurements taken by the camera are almost always overestimating the plant height. This offset is a systematic error and may come from different sources : error during depth calibration (section 3.4.3), error on the positioning of the camera above the plants or systematic error on plant measurement. As for the underestimated value, it could come from the fact that the height is computed as
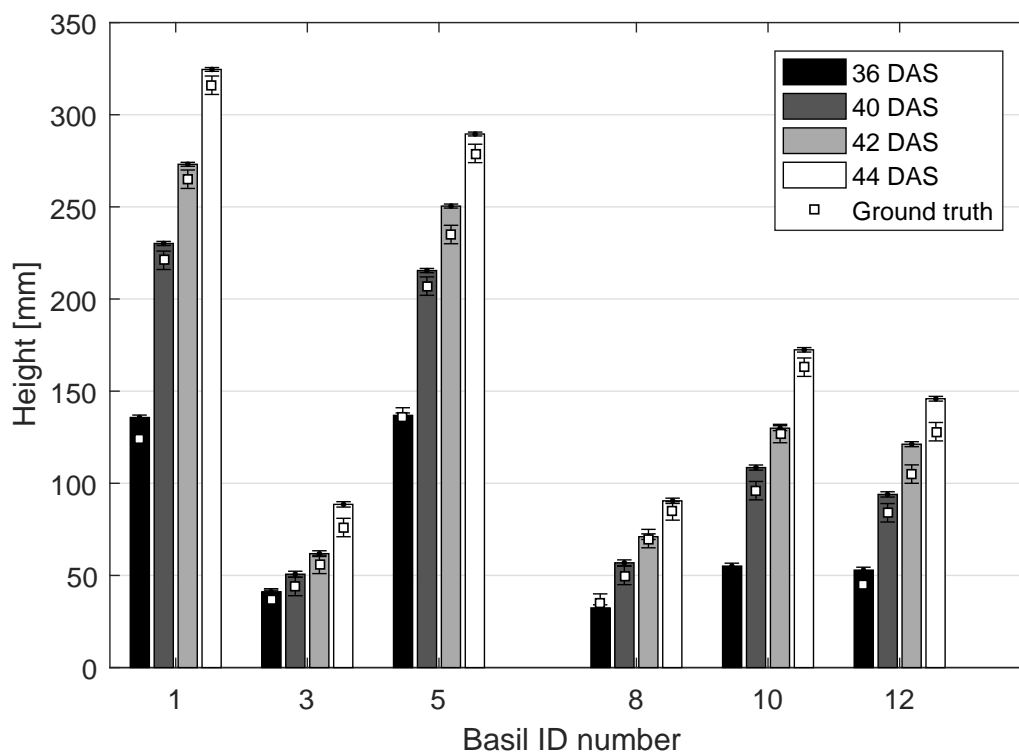
Figure 4.1 – *Heights of measured basil plants over time. Bars are grouped by plant and colors indicate different time points. Error bars on image measurement are too small to appear on graph. Error bars on measurements estimate operator-related error in the cluttered environment of the growth chamber. Plants 1-5 were part of the red light modality, and 8-12 of the blue light modality.*
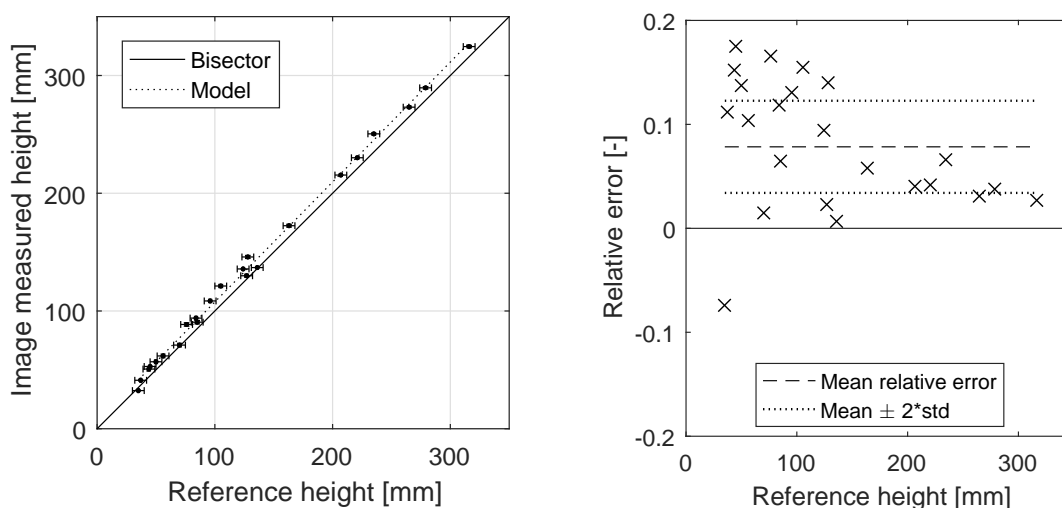
(a) *Image based height versus reference.*

$$y = 1.01 \cdot x + 6.66$$
$$R^2 = 0.997 \; ; MAE = 8.47 \, \text{mm}$$

(b) *Relative error of the height measurements.*

Figure 4.2 – *Comparison between reference values and image-based estimations. (a) : Image-based height versus reference height from manual measurements. (b) : Relative error on height measurements.*

the 99th percentile of the height points on the height maps, in a case where the measured reference height would be for example a leaf pointing upwards. The elimination of the top 1 % could eliminate the tip of the leaf, thus underestimating the height. The random component of the error is reflected by the spread of the residues. It may be due to reading errors during the manual measurements — as stated before, conditions were quite far from ideal to measure efficiently in some cases — or to the resolution of the camera. This last hypothesis seems all the more likely in the light of the fact that resolution increases with respect to distance from the camera (Figure 3.12), potentially increasing random error when estimating the height of short plants. The coefficient of determination between estimated and reference height is of 99.7 %. The MAE was computed to give a more natural quantification of the quality of the relationship between measured and reference heights than the computation of the RMSE as suggested by Willmott and Matsuura (2005). It's value is 8.47 mm. This error rate must be examined in light of the desired application, but it is important to note that Carfagni et al. (2017) mention the acquisition of filtered measurements reducing the error on measurement. A recalibration could also be considered to deal with the offset issue.

4.2 Harvest measurements

The harvest measurements comprised two main parts : the scan of individual plant organs and the reconstruction of the 3D point clouds representing the final topology of the plants.

4.2.1 Organs scans

Appendix C shows an example of a filled out scanned form.

Table 4.1 shows the difference between manually measured values and the so-called "ellipse approximations" explained in section 3.5. The sample leaves chosen to populate this table were picked to represent various shapes and sizes and go by pairs (i.e. leaves 1 and 2 come from the same node, etc.). Figure 4.3 shows an example of the segmentation result and the aforementioned ellipses, with their major and minor axes.

Table 4.1 – *Comparison between manual leaves measurements and ellipse approximation. L : length ; w : width.*

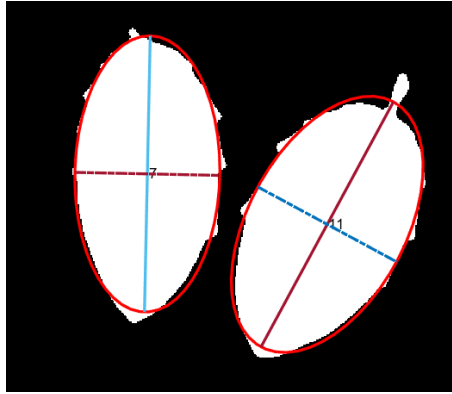| Sample	Manually measured		Ellipse approximation		Relative error	
	L [mm]	w [mm]	L [mm]	w [mm]	L [%]	w [%]
1	18,47	10,17	18,18	9,53	1,61	6,69
2	18,20	10,54	18,32	10,37	-0,66	1,63
3	50,59	33,12	50,18	29,57	0,81	12,01
4	48,79	34,71	48,09	31,97	1,46	8,57
5	60,26	60,44	60,57	59,04	-0,52	2,37
6	64,15	61,59	63,14	58,36	1,61	5,53
7	84,74	70,92	84,20	65,90	0,64	7,62
8	85,42	70,56	86,42	65,00	-1,16	8,56

Figure 4.3 – *Scanned leaves segmentation example, used to populate rows 1 and 2 of Table 4.1. The ellipses of same second-moment as the segmented leaves are plotted in red. Full lines represents the major axes and dashed lines the minor axes.*

It appears that the ellipse approximation generated very low relative errors for leaf length estimation, which is positive since it is the measurement that led us away from the bounding box approach. However, this approach performed rather poorly regarding the estimation of leaves width, with relative errors ranging up until 12 %. To counter this, two solutions can be considered :

- placing the leaves in an even more structured way such as to be able to estimate leaves width via bounding box coordinates ;
- separating the petioles from the leaves and placing them in a dedicated slot on the scan form, removing the need to use the ellipse approach and estimate all leaves dimensions via bounding box coordinates.

The analysis of leaves dimensions presented interesting results in terms of correlation between leaf length, width and area (Table 4.2). Since the leaves length and width were approximated by ellipse axes, it made sense to approximate leaf area as the area of an ellipse. Area was modeled by surface fitting against length and width (Equation 4.2). That equation is based on the relatively ellipse-like shape of basil leaves. Indeed, the regression coefficient's value is $k = 0.727$, making it very close to the actual area of an ellipse $A = \frac{\pi}{4} L w \approx 0.785 L w$ (with L = length, w = width). This relationship presents a high coefficient of determination of 99.9% and a mean absolute error of $31.2 \, \text{mm}^2$.

Table 4.2 – *Correlation matrix between leaf length, width and area.*

	Length	Width	Area
Length	1	0.97	0.95
Width	0.97	1	0.96
Area	0.95	0.96	1

$$A = k \, L \, w \tag{4.2}$$

where: A = Area [mm^2]

k = Regression coefficient [-]

L = Length [mm]

w = Width [mm]

However satisfactory this might seem, we refer the reader to Table 4.1 where it was determined that the width measurements could be improved. This relationship between actual area and leaf length and width is thus based on biased measurements but constitutes an interesting lead to pursue in a future research, in which width would be measured more accurately. An application could be to estimate leaf area in real time thanks to the SR300 based on this relationship and, for instance, the degree of curvature of leaves.

4.2.2 3D reconstruction

The leaf topology of the basil plants could be reconstructed thanks to sequential partial point cloud acquisition. To reconstruct the —almost — complete point cloud, each height map was processed and converted to point cloud format Figure 4.4. Neither stems nor petioles were detected by the camera in nadir view. All points coordinates were concatenated in a single point cloud, giving the result presented in Figure 4.5.

(a) *Leaves of node 1.*

(b) *Leaves of nodes 1 and 2.*

(c) *Leaves of nodes 2 and 3.*

(d) *Leaves of nodes 2 to 4.*
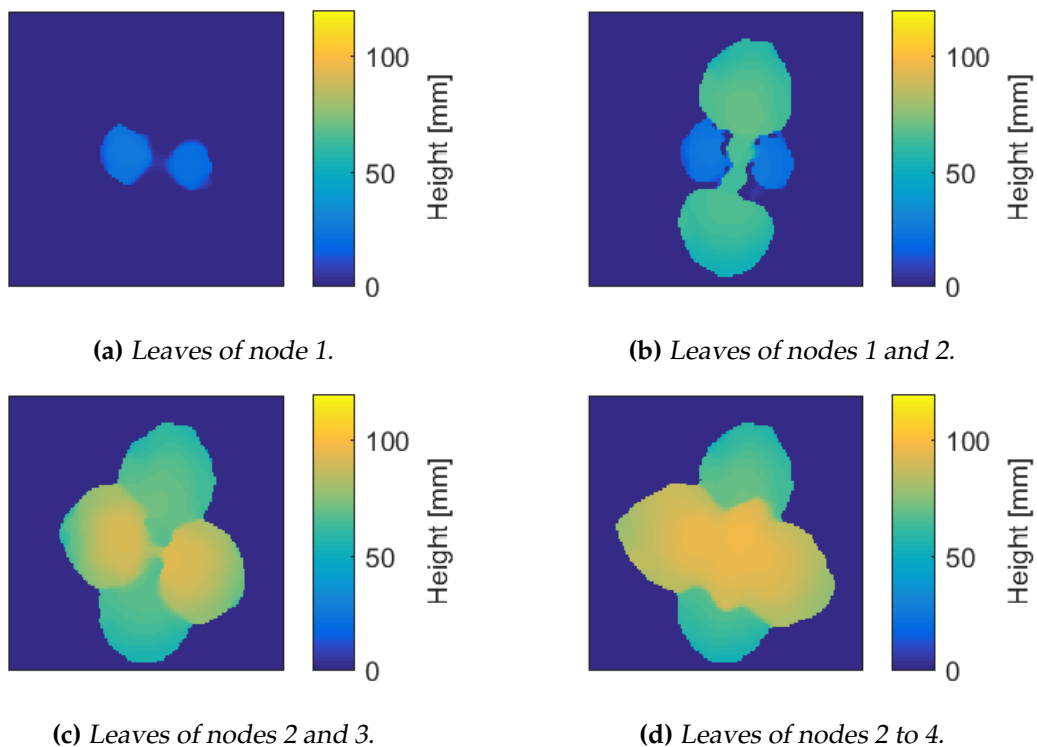
Figure 4.4 – *Height maps of the four nodes present on the plant. These are the images that were converted to 3D point clouds and assembled into a reconstructed point cloud.*

Two other views of the point cloud and the corresponding histogram of points heights is shown in Figure 4.6. The histogram counts the number of points in classes 5 mm wide. The peaks and valleys detection on the histograms shows accurate results, and allow
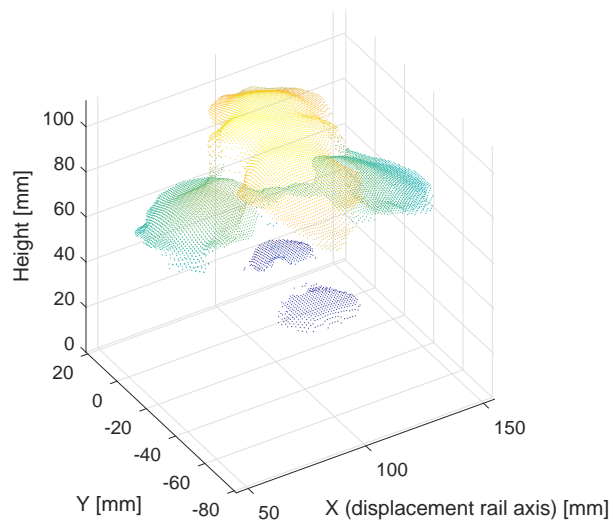
Figure 4.5 – *Raw reconstructed point cloud.*

the estimation of the height of the various nodes. The comparison between estimated internodes length and measured internode lengths are presented in Table 4.3 for three basil plants. Because of a mishap during 3D acquisition, data was lost for one basil plant. As for the two other missing plants, they had massive axillary shoots which rendered the peaks and valleys detection unusable and are not presented here. In retrospect, axillary shoots should have been pruned between frames to provide more usable data. All in all, the three remaining basil plants that were manually measured are individuals 8, 10 and 12, all part of the blue light modality.
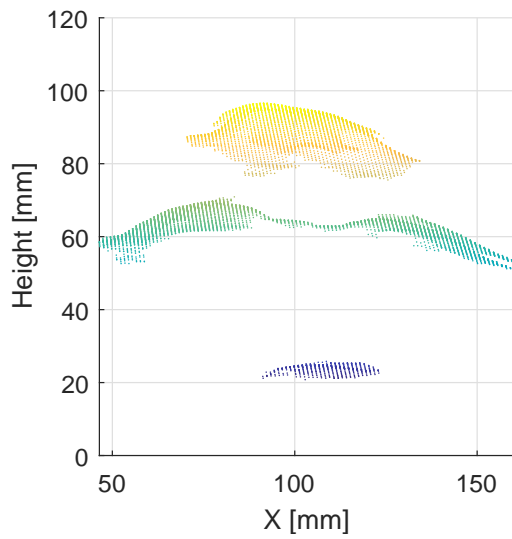
(a) *View perpendicular to X axis.*
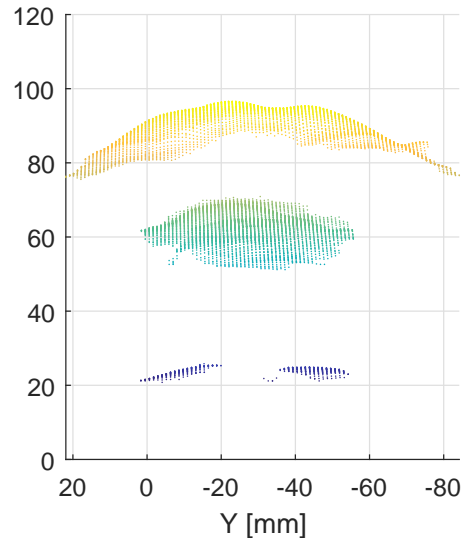
(b) *View perpendicular to Y axis.*
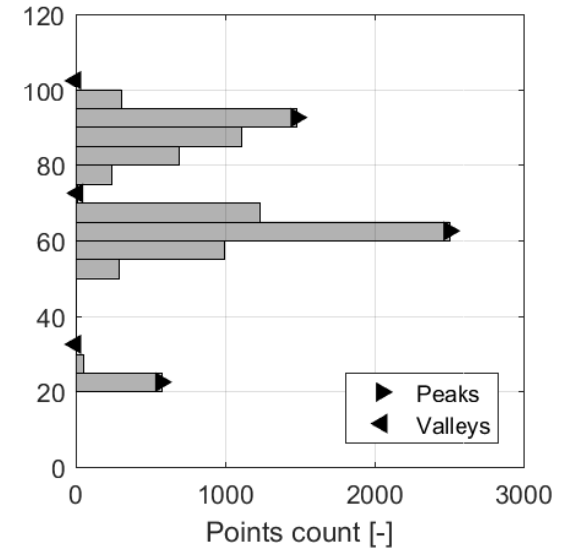
(c) *Histogram.*

Figure 4.6 – *(a,b) Point clouds of reconstructed architecture of basil n°8 from two orthogonal points of view and (c) corresponding histogram with peaks and valleys detection.*

Table 4.3 – *Comparison between estimated and measured internodes heights. Estimated height is given by histogram bins 5 mm wide, hence the ±2.5 mm uncertainty affected to the estimated values. Rows marked by a ♯ indicate leaf senescence ; the leaves did not appear at all in the point cloud.*

Basil	Internode	Estimated height [mm]±2.5 mm	Measured height [mm]	Relative error [%]
8	1	–	10.3 (♯)	–
8	2	22.5	23.3	3.6
8	3	62.5	64.6	-3.3
8	4	–	85.7	–
8	5	92.5	87.9	5.2
10	1	–	8.5	–
10	2	32.5	32.9	-1.2
10	3	102.5	105.3	-2.7
10	4	–	156.2	–
10	5	162.5	166.4	-2.3
10	6	–	168.4	–
12	1	–	8.1 (♯)	–
12	2	37.5	28.4	32.0
12	3	97.5	79.7	22.3
12	4	–	122.9	–
12	5	–	136.0	–
12	6	142.5	137.0	4.0
12	–	157.5	–	–

Results in Table 4.3 show that the estimations for internodes sometimes highly over-estimate the nodes heights, even though a manual anti-offset term was added in the computations to counter the offset mentioned in section 4.1. This is because the 3D scan detected only leaves, so the height estimation is based solely on their position and not on that of the petiole. For the case of plant 12, the high relative error rates are due to a very low insertion angle of the petioles on the stem, making the petioles almost upright, and to the inclination of the leaves that pointed upward. The point cloud thus contained all leaf points higher than the nodes, introducing bias in the histogram interpretation.

We also note that some nodes are not detected in the point cloud histogram. This is due to the insertion angle of the petiole on the stem and the inclination of leaves. Indeed, a visual analysis of the point cloud shows that the undetected storeys are in fact present, but they get mixed with neighboring nodes (see Figure 4.7b, where the leaves of the upper nodes are roughly at the same level).

4.3 Graphical representation

A practical example of the implementation of the MTG approach introduced in section 2.2 is presented in Table 4.4, in the form required to serve as input in the XPLO software. The entity column defines the ranks of the various plant components, visually by their indentation and formally by their symbolic prefix. The + symbol indicates a branching

link, and the $<$ symbol a succession link (Godin & Caraglio, 1998). Input parameters are internode length, petiole length, insertion angle on the stem and phyllotactic angle, leaf length, width, and angle relative to the horizontal. The phyllotactic angle characterizes the arrangement of the petioles around the stem. For instance, the phyllotactic angle between two opposite leaves is 180°. Figure 4.7 illustrates the graphical output of the modeling tool. The ability to reproduce a similar looking architecture validates the choice of parameters that were manually measured.

This use of the XPLO software is a premise of many possibilities. In a scenario where precise feature extraction is achieved with the help of the SR300, the extracted features could serve as input parameters for the software and generate graphical representations of plant architecture in real time. Furthermore, XPLO presents growth simulation capabilities thanks to existing plugins, and the team maintaining the software encourages the implementation of new ones (Griffon & de Coligny, 2014).
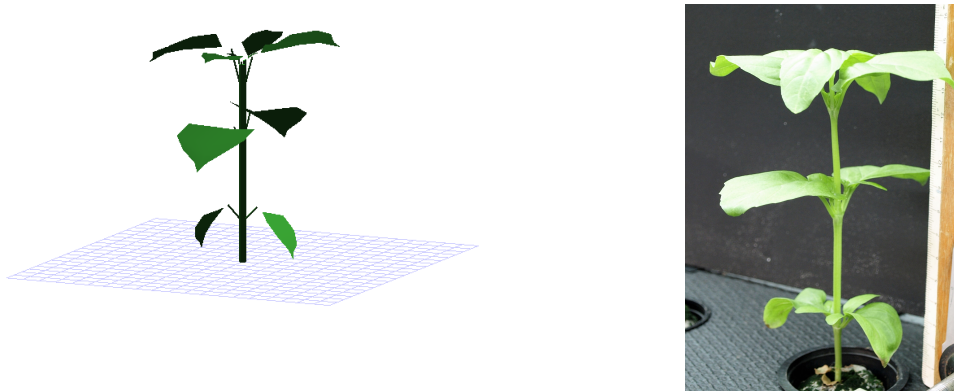
(a) *XPLO graphical representation.*   **(b)** *The real plant corresponding to the XPLO representation.*

Figure 4.7 – *XPLO graphical representation and picture of the real plant.*

Table 4.4 – *Example of MTG implementation. Input parameters are leaf length, width, petiole length and insertion angle on the stem (YIns) and phyllotactic angle (XIns).*

Entity			Name	Length [mm]	Width [mm]	YIns [°]	XIns [°]
/Scene0							
ˆ /Individual0			Indiv.				
ˆ /Axis0			Axis	1			
ˆ /Internode0			Internode	7	4		
	+petiole0		petiole	0	0	0	90
		+Leaf0	Leaf	0	0	0	
	+petiole0		petiole	0	0	0	270
		+Leaf0	Leaf	0	0	0	
ˆ <Internode0			Internode	18	4		
	+petiole0		petiole	9,9	1	45	0
		+Leaf0	Leaf	28	56	79,8	
	+petiole0		petiole	9,9	1	45	180
		+Leaf0	Leaf	33,8	50	79,2	
ˆ <Internode0			Internode	45	4		
	+petiole0		petiole	12,7	1	45	90
		+Leaf0	Leaf	49,1	92	41,5	
	+petiole0		petiole	16	1	30	270
		+Leaf0	Leaf	47	94	62,4	
ˆ <Internode0			Internode	33	4		
	+petiole0		petiole	19,3	1	15	0
		+Leaf0	Leaf	49,3	80	69,2	
	+petiole0		petiole	15,5	1	15	180
		+Leaf0	Leaf	52,4	80	46,5	
ˆ <Internode0			Internode	9	4		
	+petiole0		petiole	3	1	0	90
		+Leaf0	Leaf	48,7	42	70,8	
	+petiole0		petiole	3	1	0	270
		+Leaf0	Leaf	48,7	40	70,8	
ˆ <Internode0			Internode	1	4		
	+petiole0		petiole	3	1	0	0
		+Leaf0	Leaf	8,1	10	60,3	
	+petiole0		petiole	3	1	0	180
		+Leaf0	Leaf	8,5	10	45	

Chapter 5

Conclusion and Prospects

5.1 Conclusion

A large part of the work that went into this master's thesis was of practical nature : the development of the hydroponic system, the lighting system, the acquisition set up, the programming of the regulation systems and acquisition sequence and many efforts to try and figure out a way in the depths of the SR300 camera. Many obstacles were identified and overcome.

A depth calibration procedure was proposed, as well as a way to semi-automatically take measurements on plants after harvest. The processing of the depth frames was explored and opened some leads for the future. The AMAPstudio suite was introduced and used to reconstruct graphical representations of plants, validating the choice of parameters that were measured and the choice of the software as a representation tool, and possibly as a modeling tool in the long run.

5.2 Prospects

In view of what was accomplished during this study, a few recommendations come to mind. Table 5.1 lists the bibliographic references that contain valuable material for future research in this field.

Regarding data acquisition, a more robust set up should be implemented to handle camera malfunction, which impaired the data acquisition schedule in a major way. Another possible parameter to account for would be the light emitted by the LED array. In theory, measurements are not disturbed by light irradiation outside of the wavelength range of the IR projector, but verifying that could prove interesting in term of measurement quality assessment. Also, Wasenmüller and Stricker (2017) indicate a possible impact of sensor temperature on measurement quality for the Microsoft Kinect camera. This lead could be explored to complement the study of the SR300. As for depth calibration, the procedure could be improved by capturing several frames at each position instead of only one.

Regarding the method, it would probably be a good approach to try a 4D monitoring with more data, for example by adding a side view to the top view that was used here.

This would enable easier plant reconstruction by allowing access to plant parts that are occluded from a camera in nadir view, before attempting it with the bare minimum that is the nadir view.

In order to reconstruct plant architecture, the issue of organ multi-labeling must be adressed (Y. Li et al., 2013; Paproki et al., 2012). However, the presented techniques rely on complete plant scans, whereas our work aims to accomplish feature extraction based on partial point clouds. The acquired data can be used in a more intensive manner, with a focus on data processing instead of another master's thesis where a full experiment would have to be designed from scratch.

However, the experiment itself was not perfect and can also benefit from improvements, the major part of the hardware being already available with the prototype still in working order. The use of the SR300 for plant phenotyping purposes seems relevant, and a suitable modeling tool has been identified. All the pieces have been brought together to build an efficient phenotyping platform.

Table 5.1 – *Summary of bibliographic references of outstanding interest for future research.*

Reference	Applications
Godin and Caraglio (1998) Griffon and de Coligny (2014)	Functional structural plant modeling
Dong et al. (2016) Y. Li et al. (2013) Paproki et al. (2012) Paulus et al.	4D reconstruction and organ labeling

Bibliography

Arvidsson, S., Pérez-Rodríguez, P., & Mueller-Roeber, B. (2011). A growth phenotyping pipeline for Arabidopsis thaliana integrating image analysis and rosette area modeling for robust quantification of genotype effects. *New Phytologist*, *191*(3), 895–907. doi: 10.1111/j.1469-8137.2011.03756.x

Azzari, G., Goulden, M. L., & Rusu, R. B. (2013). Rapid characterization of vegetation structure with a microsoft kinect sensor. *Sensors (Switzerland)*, *13*(2), 2384–2398. doi: 10.3390/s130202384

Baker, N. R. (2008). Chlorophyll fluorescence: a probe of photosynthesis in vivo. *Annual review of plant biology*, *59*, 89–113. doi: 10.1146/annurev.arplant.59.032607.092759

Barthelemy, D., & Caraglio, Y. (2007, jan). Plant Architecture: A Dynamic, Multilevel and Comprehensive Approach to Plant Form, Structure and Ontogeny. *Annals of Botany*, *99*(3), 375–407. Retrieved from `https://academic.oup.com/aob/article-lookup/doi/10.1093/aob/mcl260` doi: 10.1093/aob/mcl260

Blais, F., Rioux, M., & Beraldin, J.-A. (1988, nov). Practical Considerations For A Design Of A High Precision 3-D Laser Scanner System. In R. J. Bieringer & K. G. Harding (Eds.), *Proceeding of spie* (Vol. 959, pp. 225–246). Retrieved from `http://proceedings.spiedigitallibrary.org/proceeding.aspx?articleid=1253256` doi: 10.1117/12.947787

Blanchy, G., Hubert, G., Lahaye, M., Maron, H., & Taguem, E. (2014). *Optimisation de la culture du basilic bio en CEA.* (Group project)

Carfagni, M., Furferi, R., Governi, L., Servi, M., Uccheddu, F., & Volpe, Y. (2017). On the Performance of the Intel SR300 Depth Camera : Metrological and Critical Characterization. *IEEE Sensors Journal*, *17*(14), 4508–4519. doi: 10.1109/JSEN.2017.2703829

Chen, D., Neumann, K., Friedel, S., Kilian, B., Chen, M., Altmann, T., . . . Klukas, C. (2014). Dissecting the phenotypic components of crop plant growth and drought responses based on high-throughput image analysis. *The Plant Cell Online*, *26*, 4636–4655. doi: 10.1105/tpc.114.129601

Chéné, Y., Rousseau, D., Lucidarme, P., Bertheloot, J., Caffier, V., Morel, P., . . . Chapeau-Blondeau, F. (2012). On the use of depth camera for 3D phenotyping of entire plants. *Computers and Electronics in Agriculture*, *82*, 122–127. doi: 10.1016/j.compag.2011.12.007

Dong, J., Burnham, J. G., Boots, B., Rains, G. C., & Dellaert, F. (2016). 4D Crop Monitoring: Spatio-Temporal Reconstruction for Agriculture. *IEEE International Conference on Robotics and Automation.* Retrieved from `http://arxiv.org/abs/1610.02482`

Fahlgren, N., Gehan, M. A., & Baxter, I. (2015). Lights, camera, action : high-throughput plant phenotyping is ready for a close-up. *Current Opinion in Plant Biology*, *24*, 93–99. Retrieved from `http://dx.doi.org/10.1016/j.pbi.2015.02.006` doi: 10.1016/j.pbi.2015.02.006

Fiorani, F., & Schurr, U. (2013). Future Scenarios for Plant Phenotyping. *Annu. Rev. Plant Biol*, *64*(February), 267–91. Retrieved from `www.annualreviews.org` doi: 10.1146/annurev-arplant-050312-120137

Folta, K. M., & Childers, K. S. (2008). Light as a growth regulator: Controlling plant biology with narrow-bandwidth solid-state lighting systems. *HortScience*, *43*(7), 1957–1964. doi: 10.1186/1471-2164-12-360

Fraden, J. (2010). *Handbook of modern sensors : physics, designs, and applications*. New York: Springer Verlag.

Godfray, H. C. J., Beddington, J. R., Crute, I. R., Haddad, L., Lawrence, D., Muir, J. F., ... Toulmin, C. (2012). The Challenge of Food Security. *Science*, *327*(February), 812–818. Retrieved from `http://www.elgaronline.com/view/9780857939371.xml` doi: 10.4337/9780857939388

Godin, C., & Caraglio, Y. (1998, mar). A Multiscale Model of Plant Topological Structures. *Journal of Theoretical Biology*, *191*(1), 1–46. Retrieved from `http://linkinghub.elsevier.com/retrieve/pii/S0022519397905610` doi: 10.1006/jtbi.1997.0561

Golzarian, M. R., Frick, R. a., Rajendran, K., Berger, B., Roy, S., Tester, M., & Lun, D. S. (2011). Accurate inference of shoot biomass from high-throughput images of cereal plants. *Plant methods*, *7*, 2. doi: 10.1186/1746-4811-7-2

Griffon, S., & de Coligny, F. (2014). AMAPstudio : An editing and simulation software suite for plants architecture modelling. *Ecological Modelling*, *290*, 3–10. doi: 10.1016/j.ecolmodel.2013.10.037

Guidi, G., Gonizzi, S., & Micoli, L. (2016). 3D capturing performances of low-cost range sensors for mass-market applications. *International Archives of the Photogrammetry, Remote Sensing and Spatial Information Sciences - ISPRS Archives*, *41*(July), 33–40. doi: 10.5194/isprsarchives-XLI-B5-33-2016

Henke, M., Kurth, W., & Buck-Sorlin, G. H. (2016, dec). FSPM-P: towards a general functional-structural plant model for robust and comprehensive model development. *Frontiers of Computer Science*, *10*(6), 1103–1117. Retrieved from `http://link.springer.com/10.1007/s11704-015-4472-8` doi: 10.1007/s11704-015-4472-8

Jones, H. G., Serraj, R., Loveys, B. R., Xiong, L., Wheaton, A., & Price, A. H. (2009). Thermal infrared imaging of crop canopies for the remote diagnosis and quantification of plant responses to water stress in the field. *Functional Plant Biology*, *36*(11), 978–989. doi: 10.1071/FP09123

Kalantar-zadeh, K. (2013). *Sensors*. Boston, MA: Springer US. Retrieved from `http://ebooks.cambridge.org/ref/id/CBO9781107415324A009{%}5Cnhttp://link.springer.com/10.1007/978-1-4614-5052-8http://link`

`.springer.com/10.1007/978-1-4614-5052-8` doi: 10.1007/978-1-4614 -5052-8

Kautsky, H., & Hirsch, A. (1931). Neue Versuche zur Kohlensäureassimilation. *Die Naturwissenschaften*, *19*(48), 964. doi: 10.1007/BF01516164

Kozai, T. (2016). *Led lighting for urban agriculture*. Singapore: Springer.

Leemans, V., Marlier, G., Destain, M.-F., Dumont, B., & Mercatoris, B. (2017). Estimation of leaf nitrogen concentration on winter wheat by multispectral imaging. , *10213*, 102130I. Retrieved from `http://proceedings.spiedigitallibrary.org/ proceeding.aspx?doi=10.1117/12.2268398` doi: 10.1117/12.2268398

Li, L., Zhang, Q., & Huang, D. (2014). A review of imaging techniques for plant phenotyping. *Sensors (Switzerland)*, *14*(11), 20078–20111. doi: 10.3390/s141120078

Li, Y., Fan, X., Mitra, N. J., Chamovitz, D., Cohen-Or, D., & Chen, B. (2013). Analyzing growing plants from 4D point cloud data. *ACM Transactions on Graphics*, *32*(6), 1–10. Retrieved from `http://dl.acm.org/ citation.cfm?doid=2508363.2508368{%}5Cnpapers3://publication/ doi/10.1145/2508363.2508368` doi: 10.1145/2508363.2508368

Liaros, S., Botsis, K., & Xydis, G. (2016). Technoeconomic evaluation of urban plant factories: The case of basil (Ocimum basilicum). *Science of the Total Environment*, *554-555*, 218–227. Retrieved from `http://dx.doi.org/10.1016/j.scitotenv.2016 .02.174` doi: 10.1016/j.scitotenv.2016.02.174

LibRealSense. (2017). *Librealsense : Cross-platform api for intel realsense devices*. GitHub repository. Retrieved from `https://github.com/IntelRealSense/ librealsense`

Lobet, G., Draye, X., & Périlleux, C. (2013). An online database for plant image analysis software tools An online database for plant image analysis software tools. *Plant methods*, *9*, 1–7. doi: 10.1186/1746-4811-9-38

Marti, J., Bort, J., Slafer, G. A., & Araus, J. L. (2007). Can wheat yield be assessed by early measurements of Normalized Difference Vegetation Index? *Annals of Applied Biology*, *150*(2), 253–257. doi: 10.1111/j.1744-7348.2007.00126.x

Najla, S., Vercambre, G., Pagès, L., Grasselly, D., Gautier, H., & Génard, M. (2009, oct). Tomato plant architecture as affected by salinity: Descriptive analysis and integration in a 3-D simulation model. *Botany*, *87*(10), 893–904. Retrieved from `http://www.nrcresearchpress.com/doi/abs/10.1139/B09-061` doi: 10 .1139/B09-061

Paproki, A., Sirault, X. R. R., Berry, S., Furbank, R. T., & Fripp, J. (2012). A novel mesh processing based technique for 3D plant analysis. *BMC Plant Biology*, *12*(1), 63. Retrieved from `http://www.biomedcentral.com/1471-2229/12/63` doi: 10.1186/1471-2229-12-63

Paulus, S., Behmann, J., Mahlein, A. K., Plümer, L., & Kuhlmann, H. (2014). Low-cost 3D systems: Suitable tools for plant phenotyping. *Sensors (Switzerland)*. doi: 10.3390/s140203001

Paulus, S., Dupuis, J., Mahlein, A.-K., & Kuhlmann, H. (2013). Surface feature based

classification of plant organs from 3D laserscanned point clouds for plant phenotyping. *BMC Bioinformatics*, *14*. Retrieved from `http://www.biomedcentral.com/1471-2105/14/238`

Paulus, S., Schumann, H., Kuhlmann, H., & Léon, J. (2014, may). High-precision laser scanning system for capturing 3D plant architecture and analysing growth of cereal plants. *Biosystems Engineering*, *121*, 1–11. Retrieved from `http://linkinghub.elsevier.com/retrieve/pii/S1537511014000166` doi: 10 .1016/j.biosystemseng.2014.01.010

Rovira-Más, F., Zhang, Q., & Reid, J. F. (2005). Creation of three-dimensional crop maps based on aerial stereoimages. *Biosystems Engineering*, *90*(3), 251–259. doi: 10.1016/j.biosystemseng.2004.11.013

Rusu, R., Blodow, N., Marton, Z., Soos, A., & Beetz, M. (2007). Towards 3D Object Maps for Autonomous Household Robots. *Iros '07*, 3191–3198. Retrieved from `http://ieeexplore.ieee.org/lpdocs/epic03/wrapper.htm?arnumber=4399309` doi: 10.1109/IROS.2007.4399309

United Nations. (2017). *World Population Prospects: The 2017 Revision, Key Findings and Advance Tables* (Tech. Rep.).

Wasenmüller, O., & Stricker, D. (2017). Comparison of Kinect V1 and V2 Depth Images in Terms of Accuracy and Precision. In (pp. 34–45). Retrieved from `http://link.springer.com/10.1007/978-3-319-54427-4{_}3` doi: 10.1007/978 -3-319-54427-4_3

Wikipedia. (2017). *Nadir — Wikipedia, the free encyclopedia.* `http://en.wikipedia.org/w/index.php?title=Nadir&oldid=794800554`. (Online; accessed July 2017)

Willmott, C. J., & Matsuura, K. (2005). Advantages of the mean absolute error (MAE) over the root mean square error (RMSE) in assessing average model performance. *Climate Research*, *30*(1), 79–82. doi: 10.3354/cr030079

Woebbecke, D., Meyer, G., Von Bargen, K., & Mortensen, D. (1995). Color indices for weed identification under various soil, residue, and lighting conditions. *Transactions of the ASAE*, *38*(1), 259–269. Retrieved from `http://cat.inist.fr/?aModele=afficheN{&}cpsidt=3503524` doi: 10.13031/2013.27838

Zanuttigh, P., Marin, G., Dal Mutto, C., Dominio, F., Minto, L., & Cortelazzo, G. M. (2016). *Time-of-Flight and Structured Light Depth Cameras*. Cham: Springer International Publishing. Retrieved from `http://link.springer.com/10.1007/978-3-319-30973-6` doi: 10.1007/978-3-319-30973-6

Zhang, Z. (2002). A Flexible New Technique for Camera Calibration (Technical Report). *IEEE Transactions on Pattern Analysis and Machine Intelligence*, *22*(11), 1330–1334. doi: 10.1109/34.888718

Appendix A

LED intensity control

```python
#!/bin/env python

import serial
import time
import io
import numpy as np


def openSerial():
    ser = serial.Serial('/dev/ttyUSB0')  # open serial port
    print(ser.name)          # check which port was really used
    ser.baudrate = 115200
    ser
    return ser

def closeSerial():
    ser.close() # close port

def setDMX(channelStr, intensity, ser, t_pause): # select the DMX channel
    if channelStr == 'r':
        channel = range(9,17)
    elif channelStr == 'b':
        channel = range(1,9)
    elif channelStr == 'w':
        channel = range(17,33)
    elif channelStr == 'all':
        channel = range(1,33)

    sz = len(channel) ;

    for i in np.nditer(channel,op_flags=['readonly']) : # set the ...
        intensity for the channel
        for j,value in np.ndenumerate(i) :
            intensiteToInt = intensity[0,j]
            intensityToInt = intensityToInt.item(0)
            strWrite = 's{}v{}'.format(i[j[0]],intensityToInt )
            print(strWrite)
            ser.write('b{}\r'.format(strWrite))

def zeroslistmaker(n):
    return [0] * n

def oneslistmaker(n):
    return [1] * n
```

```python
44
45  t_pause = .1
46
47  ser = openSerial()
48
49
50  # blue channels (8)
51  intensity = np.matrix( (200, 200, 200, 200, 0, 0, 0, 0) )  # definition ...
        of wanted intensity in selected channels
52  setDMX('b', intensity, ser, t_pause)
53
54  # red channels (8)
55  intensity = np.matrix( (0, 0, 0, 0, 200, 200, 200, 200) )
56  setDMX('r', intensity, ser, t_pause)
57
58  # white channels (16)
59  intensity = np.matrix( (100, 100, 100, 100, 100, 100, 100, 100, 100, ...
        100, 100, 100, 100, 100, 100, 100) )
60  setDMX('w', intensity, ser, t_pause)
61
62  closeSerial()
63  print('%%%%%  DONE  %%%%%')
64
65  import sys
66  sys.exit()
```

Appendix B

Basil scan form

The form used to lay out and scan plant material is presented on the next page.

The header contains measurement metadata :

- batch number ;
- plant ID ;
- checkbox to make sure that side view RGB pictures were indeed taken ;
- color recipe ;
- page number / total pages number for the plant ;
- date.

Black crosses are present in the corners, with their respective center at known distances (17.5 cm horizontally, 26.6 cm vertically) to compute the scale factor between pixels and real-world units for image analysis measurements, in the case where image resolution is not known. If it is known, the computation of the scale factor is trivial as it is given by the number of dots per inch.

The rest of the grid is annotated.

+   +

Batch : __   ID : __   Sideways pic □   Modality : □ red □ blue   Page : _ /_   Date : 201_ / __ / __

ID	Leaves and internodes	Shoots	Infos
[internode ID number]	*[leaves]* *[internode]*	*[shoots]*	Mass [g] = L [mm] = l [mm] =
[internode ID number]	*[leaves]* *[internode]*	*[shoots]*	Mass [g] = L [mm] = l [mm] =

+   +

Appendix C

Example of full scan form

On the next page is displayed a full scan form. All plant material was laid flat in a similar manner, with incisions to ensure the flatness of the leaves. Some reflections are present on the resulting image because of the plastic covering the leaves and internodes but they did not impair the quality of the image analysis.

Figure C.1 – *Full scan form for batch 4, plant 8, modality = blue, page $2/3$ at the date of the end of the experiment : July 7th, 2017.*